Title

A C19MC-LIN28A-MYCN Oncogenic Circuit Driven by Hijacked Super-enhancers Is a Distinct Therapeutic Vulnerability in ETMRs: A Lethal Brain Tumor

Journal

Cancer Cell, 36(1)

ISSN

1535-6108

Authors

Sin-Chan, Patrick
Mumal, Iqra
Suwal, Tannu
et al.

Publication Date

2019-07-01

DOI

10.1016/j.ccell.2019.06.002

Peer reviewed

Article

Cancer Cell

A *C19MC*-LIN28A-MYCN Oncogenic Circuit Driven by Hijacked Super-enhancers Is a Distinct Therapeutic Vulnerability in ETMRs: A Lethal Brain Tumor

Graphical Abstract

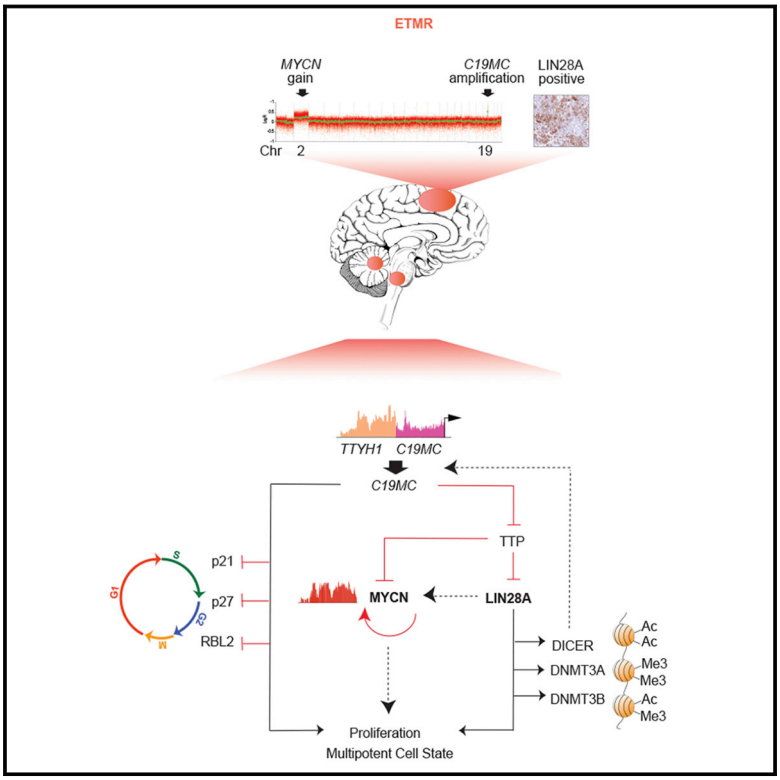

Highlights

- *C19MC* alterations and chr2 gains comprise the most frequent genetic events in ETMRs
- *C19MC-TTYH1* gene fusion and MYCN DNA interactions create super-enhancers
- Super-enhancers and multiple feedback loops fortify a *C19MC*-LIN28A-MYCN circuitry
- BET domain inhibitors abrogate *C19MC*-LIN28A-MYCN circuit to induce ETMR cell death

Authors

Patrick Sin-Chan, Iqra Mumal, Tannu Suwal, ..., Stephen C. Mack, Jeremy N. Rich, Annie Huang

Correspondence

annie.huang@sickkids.ca

In Brief

Sin-Chan et al. uncover a *C19MC*-LIN28A-MYCN super-enhancer-dependent oncogenic circuit in embryonal tumors with multilayered rosettes (ETMRs). The circuit entraps an early neural lineage network to sustain embryonic epigenetic programming and is vulnerable to bromodomain inhibition, which promotes ETMR cell death.

Sin-Chan et al., 2019, Cancer Cell *36*, 51–67
July 8, 2019
https://doi.org/10.1016/j.ccell.2019.06.002

CellPress

CellPress

A *C19MC*-LIN28A-MYCN Oncogenic Circuit Driven by Hijacked Super-enhancers Is a Distinct Therapeutic Vulnerability in ETMRs: A Lethal Brain Tumor

Patrick Sin-Chan,[1,43] Iqra Mumal,[1,2,43] Tannu Suwal,[1,2] Ben Ho,[1] Xiaolian Fan,[1] Irtisha Singh,[3] Yuchen Du,[4] Mei Lu,[1] Neilket Patel,[1] Jonathon Torchia,[5] Dean Popovski,[1] Maryam Fouladi,[6] Paul Guilhamon,[7] Jordan R. Hansford,[8] Sarah Leary,[9] Lindsey M. Hoffman,[10] Jean M. Mulcahy Levy,[10] Alvaro Lassaletta,[11] Palma Solano-Paez,[12] Eloy Rivas,[13] Alyssa Reddy,[14] G. Yancey Gillespie,[15] Nalin Gupta,[16] Timothy E. Van Meter,[17] Hideo Nakamura,[18] Tai-Tong Wong,[19] Young-Shin Ra,[20] Seung-Ki Kim,[21] Luca Massimi,[22] Richard G. Grundy,[23] Jason Fangusaro,[24] Donna Johnston,[25] Jennifer Chan,[26] Lucie Lafay-Cousin,[27] Eugene I. Hwang,[28] Yin Wang,[29] Daniel Catchpoole,[30] Jean Michaud,[31]

(Author list continued on next page)

[1]Arthur and Sonia Labatt Brain Tumor Research Centre, Division of Haematology/Oncology, Hospital for Sick Children, Toronto, ON M5G0A4, Canada
[2]Department of Laboratory Medicine and Pathobiology, Faculty of Medicine, University of Toronto, Toronto, ON M5S1A8, Canada
[3]Department of Molecular and Human Genetics, Baylor College of Medicine, Houston, TX 77030, USA
[4]Department of Pediatrics, Division of Hematology and Oncology, Baylor College of Medicine, Texas Children's Hospital, Houston, TX 77030, USA
[5]Princess Margaret Cancer Center-OICR Translational Genomics Laboratory, Ontario Institute for Cancer Research, Toronto, ON M5G0A3, Canada
[6]Division of Oncology, Department of Cancer and Blood Diseases, Cincinnati Children's Hospital, Cincinnati, OH 45229, USA
[7]Developmental and Stem Cell Biology Program and Arthur and Sonia Labatt Brain Tumor Research Centre, The Hospital for Sick Children, Toronto, ON M5G0A4, Canada
[8]Children's Cancer Centre, Royal Children's Hospital, Murdoch Children's Research Institute, Department of Pediatrics, University of Melbourne, Melbourne, VIC 3052, Australia
[9]Department of Hematology-Oncology, Seattle Children's Hospital, Seattle, WA 98105, USA
[10]Department of Pediatrics, University of Colorado Denver, Aurora, CO 80045, USA
[11]Pediatric Hematology and Oncology Department, Hospital Infantil Universitario Niño Jesús, Madrid 28009, Spain

(Affiliations continued on next page)

SUMMARY

Embryonal tumors with multilayered rosettes (ETMRs) are highly lethal infant brain cancers with characteristic amplification of Chr19q13.41 miRNA cluster (*C19MC*) and enrichment of pluripotency factor LIN28A. Here we investigated *C19MC* oncogenic mechanisms and discovered a *C19MC*-LIN28A-MYCN circuit fueled by multiple complex regulatory loops including an MYCN core transcriptional network and super-enhancers resulting from long-range *MYCN* DNA interactions and *C19MC* gene fusions. Our data show that this powerful oncogenic circuit, which entraps an early neural lineage network, is potently abrogated by bromodomain inhibitor JQ1, leading to ETMR cell death.

INTRODUCTION

Embryonal brain tumors, the largest category of malignant brain tumors diagnosed in children 0–14 years of age, comprise a molecular and histologic spectrum of diseases that include medulloblastoma, rhabdoid tumors, and a more recently discovered tumor entity, embryonal tumors with multilayered rosettes (ETMRs), which were first identified based on recurrent

Significance

ETMRs are distinctly challenging brain tumors of infants and very young children, with characteristic rapid progression and only 10%–20% overall survival. Since the discovery of *C19MC*, an embryonic stem cell-enriched, primate-specific miRNA cluster, as a disease marker of ETMR, there has been limited progress in biological and therapeutic understanding of this disease. Here we show that tumor-specific genomic and epigenomic alterations of *C19MC* entraps and drives multiple feedforward loops to fuel a potent *C19MC*-LIN28A-MYCN oncogenic circuit, which can be powerfully abrogated by bromodomain inhibitors. Our findings underscore *C19MC* as a critical oncogene in ETMRs and provide critical therapeutic insights and a framework for developing high-fidelity models for this orphan disease.

Benjamin Ellezam,[32] Ramya Ramanujachar,[33] Holly Lindsay,[4] Michael D. Taylor,[2,34] Cynthia E. Hawkins,[2,35] Eric Bouffet,[36] Nada Jabado,[37] Sheila K. Singh,[38] Claudia L. Kleinman,[37] Dalia Barsyte-Lovejoy,[39] Xiao-Nan Li,[4,40] Peter B. Dirks,[2,34] Charles Y. Lin,[3] Stephen C. Mack,[4] Jeremy N. Rich,[41] and Annie Huang[1,2,36,42,44,*]

[12]Department of Pediatric Oncology, Hospital Infantil Virgen del Rocio, Seville 41013, Spain
[13]Department of Pathology, Neuropathology Division, Hospital Universitario Virgen del Rocio, Seville 41013, Spain
[14]University of Alabama at Birmingham, Birmingham, AL 35294, USA
[15]Department of Neurosurgery, University of Alabama at Birmingham, Birmingham AL 35294, USA
[16]Department of Neurological Surgery, University of California, San Francisco, CA 94143-0112, USA
[17]Department of Pediatrics, Virginia Commonwealth University, Richmond, VA 23298-0631, USA
[18]Department of Neurosurgery, Kurume University, Fukuoka 830-0011, Japan
[19]Pediatric Brain Tumor Program, Taipei Cancer Center, Taipei Medical University, Taipei 11031, Taiwan
[20]Department of Neurosurgery, Asan Medical Center, Seoul 138-736, Korea
[21]Division of Pediatric Neurosurgery, Seoul National University Children's Hospital, Seoul 03080, Korea
[22]Department of Neurosurgery, Fondazione Policlinico A. Gemelli IRCCS, Università Cattolica del Sacro Cuore, Rome 00168, Italy
[23]Children's Brain Tumor Research Centre, Queen's Medical Centre University of Nottingham, Nottingham NG72UH, UK
[24]Department of Pediatric Hematology and Oncology at Children's Healthcare of Atlanta and the Emory University School of Medicine, Atlanta, GA 30322, USA
[25]Division of Hematology/Oncology, Children's Hospital of Eastern Ontario, Ottawa, ON K1H8L1, Canada
[26]Department of Pathology and Laboratory Medicine, University of Calgary, Calgary, AB T2N1N4, Canada
[27]Department of Pediatric Oncology, Alberta Children's Hospital, Calgary, AB T3B6A8, Canada
[28]Center for Cancer and Blood Disorders, Children's National Medical Center, Washington, DC 20010, USA
[29]Department of Neuropathology Huashan Hospital, Fudan University, Shanghai 200040, China
[30]The Tumor Bank, Children's Cancer Research Unit, Kids Research, the Children's Hospital at Westmead, Westmead, NSW 2145, Australia
[31]Department of Pathology and Laboratory Medicine, University of Ottawa, Ottawa, ON K1H8M5, Canada
[32]Department of Pathology, CHU Sainte-Justine Research Center, Université de Montréal, Montréal, QC H3T1C5, Canada
[33]Paediatric Haematology and Oncology, Southampton Children's Hospital, Southampton SO166YD, UK
[34]Arthur and Sonia Labatt Brain Tumor Research Centre, Division of Neurosurgery, Hospital for Sick Children, Toronto, ON M5G0A4, Canada
[35]Department of Pathology, The Hospital for Sick Children, Toronto, ON M5G1X8, Canada
[36]Division of Hematology-Oncology, The Hospital for Sick Children, Department of Pediatrics, University of Toronto, Toronto, ON M5G0A4, Canada
[37]Departments of Pediatrics and Human Genetics, McGill University, Montréal, QC H3A0C7, Canada
[38]McMaster Stem Cell and Cancer Research Institute, McMaster University, Hamilton, ON L8S4K1, Canada
[39]Structural Genomics Consortium, University of Toronto, Toronto, ON M5G1L7, Canada
[40]Department of Pediatrics, Feinberg School of Medicine, Northwestern University, Chicago, IL 60611, USA
[41]Department of Medicine, Division of Regenerative Medicine, University of California, San Diego, CA 92093, USA
[42]Department of Medical Biophysics, Faculty of Medicine, University of Toronto, Toronto, ON M5G1L7, Canada
[43]These authors contributed equally
[44]Lead Contact
*Correspondence: annie.huang@sickkids.ca
https://doi.org/10.1016/j.ccell.2019.06.002

amplification of the *C19MC* miRNA cluster on Chr19q13.41 (Li et al., 2009). Subsequent studies revealed a spectrum of embryonal brain tumors previously categorized as distinct histologic entities that exhibited overlapping molecular features, which led to the categorization of *C19MC*-altered embryonal tumors as a single diagnostic entity in the revised 2016 World Health Organization CNS tumor classification (Louis et al., 2016). ETMRs are now increasingly recognized as a distinctly aggressive brain tumor arising in infants and young children <4 years old with long-term survival of only 10%–20% (Korshunov et al., 2014; Li et al., 2009; Spence et al., 2014b). To date, biological and therapeutic studies of this orphan disease has been significantly limited by a paucity of experimental and therapeutic models.

C19MC, which is the largest primate-specific miRNA cluster, encodes 54 miRNAs normally expressed in placental and germinal tissues (Bentwich et al., 2005; Bortolin-Cavaille et al., 2009). ETMRs exhibit histologic features reminiscent of early neural tube development and are transcriptionally enriched for genes with functions in early neural differentiation, including *LIN28A*, *POU3F2*, *MEIS1/2*, and *SOX3* (Li et al., 2009; Pfister et al., 2009; Picard et al., 2012), suggesting early neural progenitor origins. Significantly, ETMR RNA sequencing (RNA-seq) studies revealed fusion of *C19MC* to the promoter of *TTYH1* (an embryonic chloride channel protein), and correlated *C19MC* miRNA expression with enrichment of an early neural-restricted isoform of the *de novo* DNA methyltransferase, *DNMT3B6* (Kleinman et al., 2014). These observations, along with our previous demonstration that *C19MC* oncogenic miRNAs (oncomiRs) modulates human neural stem cell (hNSC) growth and differentiation (Li et al., 2009), suggests that *C19MC* may promote or maintain a primitive neural/embryonic epigenetic cell phenotype in ETMRs. However, oncogenic mechanisms and gene targets of *C19MC* remain elusive.

ETMR transcriptional signatures are enriched for high expression of LIN28A, a pluripotency factor and RNA-binding protein, which is implicated in neural development and in the pathogenesis of other advanced cancers (Viswanathan et al., 2009). Notably, LIN28A is highly expressed in a small proportion of embryonal tumors with transcriptional and epigenetic features of ETMRs without evident *C19MC* alterations or expression, indicating an important role for this oncogene in ETMR pathogenesis

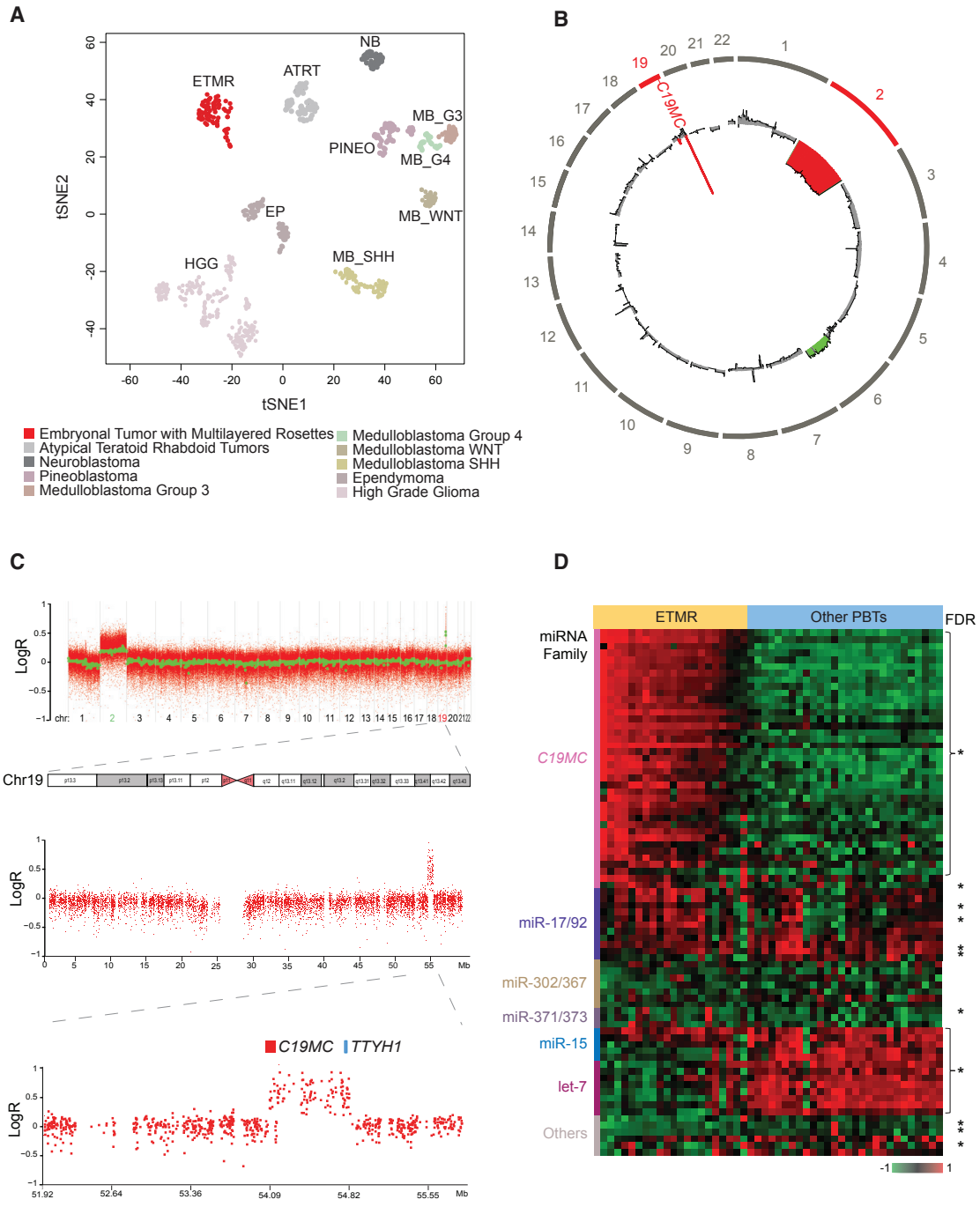

Figure 1. Global Molecular Features of ETMRs

(A) t-SNE visualization of unsupervised cluster analyses of 850k Illumina methylation array data from ETMRs (n = 80) and a reference dataset of childhood brain tumors and neuroblastoma (n = 643).

(B) Circos plot of global methylation-based copy-number profiles in ETMRs. Regions of amplification/gains and losses are respectively highlighted in red and green.

(C) High-resolution SNP copy-number profiles generated using allele-specific copy-number analysis of tumors in a representative ETMR with focal Chr19q13.42 amplification encompassing *C19MC* (red) and *TTYH1* (blue) shown in zoomed-in view.

(D) Heatmap of NanoString (v.3) miRNA expression data from 21 ETMRs and 28 other PBTs showing the top 20% of miRNAs enriched in ETMRs; *q < 0.05. FDR, false discovery rate. See also Figure S1 and Table S1.

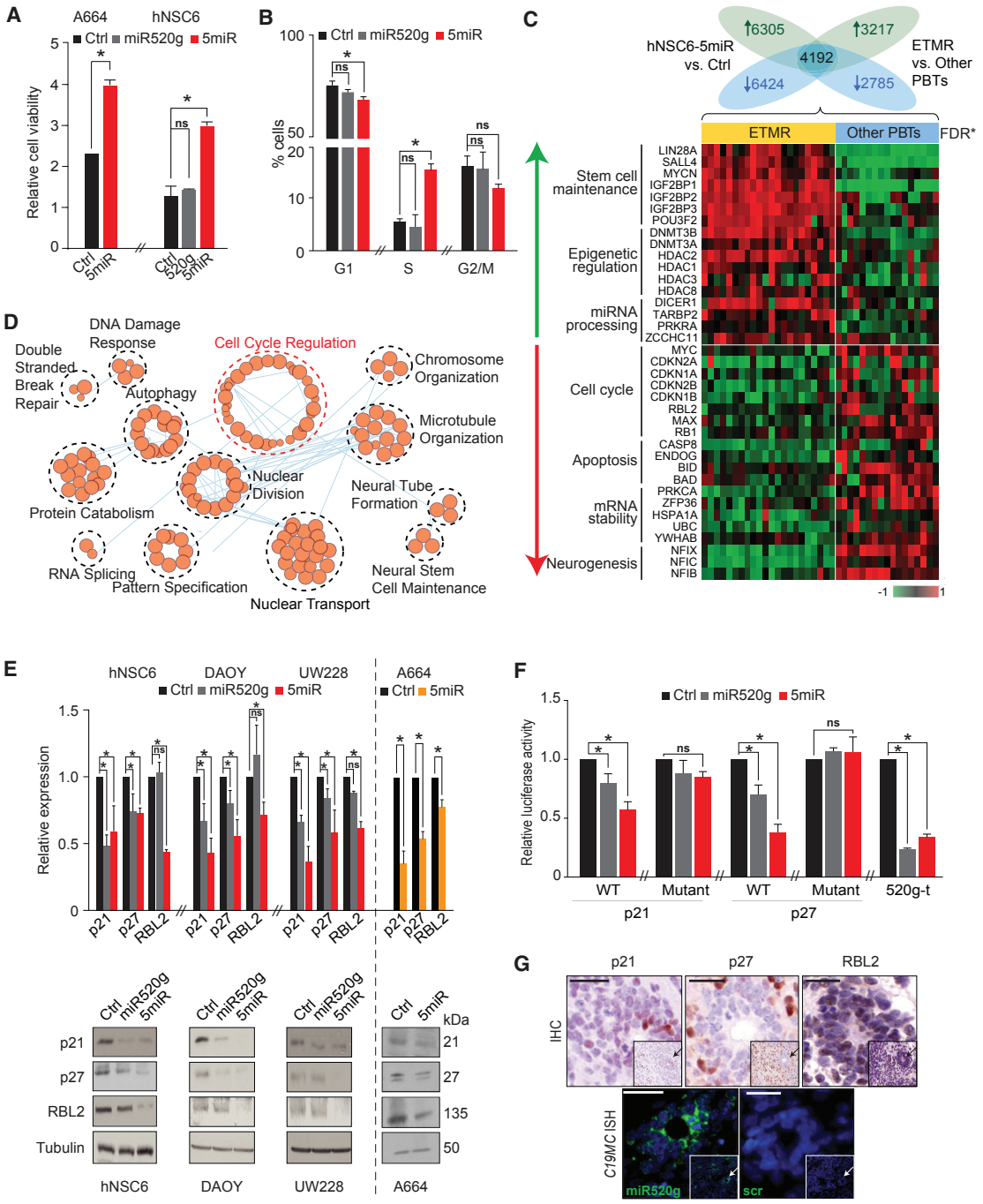

Figure 2. *C19MC* oncomiRs Cooperatively Target Multiple Cell-Cycle Tumor Suppressors

(A) Cell viability assays of A664-5miR, hNSC6-5miR, hNSC6-miR520g, and control cell lines 5 days post-seeding.

(B) Cell-cycle analysis of hNSC6-5miR, hNSC6-miR520g, and control cell lines 5 days post-seeding; proportion of cells relative to total cell numbers are shown.

(C) Schema of integrated differential RNA-seq analyses comparing hNSC6-5miR versus vector control cell lines (n = 2) and primary ETMRs (n = 22) versus other PBTs (n = 17); number of significantly up-, downregulated, and common *C19MC* responsive genes (FC > 1.2, <−1.2; *q < 0.05) are shown. Heatmap shows relative expression of select genes from the most highly ranked biological processes in ETMRs versus other PBTs identified using pathway analyses of 4,192 *C19MC* responsive genes; *q < 0.05.

(D) Cytoscape visualization of biological processes (*q < 0.05) represented by the 4,192 genes identified in (C). Nodes represent related enriched gene sets, node size corresponds to total gene numbers.

(E) qRT-PCR and western blot analyses of hNSC6, Daoy, UW228, and A664 cell lines with miR520g and 5miR expression, is shown relative to corresponding vector control lines.

(legend continued on next page)

(Korshunov et al., 2014; Spence et al., 2014b). In this study, we sought to define downstream targets and oncogenic mechanisms of *C19MC*, and to elucidate the functional relationship of *C19MC* and LIN28A in ETMR transformation.

RESULTS

Recurrent Chromosome 2 and 19 Copy-Number Alterations Are Hallmarks of ETMRs

The molecular landscape and pathogenesis of ETMRs remain largely unknown, as few of these tumor entities have been extensively characterized. To begin to elucidate mechanisms of ETMR pathogenesis, we examined 80 primary ETMRs using integrated global methylation, SNP, transcriptional, and miRNA profiling (Table S1). Methylation and transcriptional profiling showed ETMRs are distinct from other pediatric brain tumors (PBTs), notably embryonal brain tumors, including rhabdoid tumors, pineoblastoma and medulloblastoma (Louis et al., 2016) (Figure 1A). Transcriptional analyses confirmed characteristic enrichment of stem cell maintenance and early neural/embryonic developmental pathways in ETMRs. Copy-number analyses using methylation and Omni SNP array data showed that Chr2 gains (77.5%) and focal Chr19 alterations (80%) centered on *C19MC* were the most frequent copy-number aberrations (CNA) and were concurrently present in 65% of ETMRs (Figures 1B and S1A–S1C). Detailed methylation/SNP (n = 80) and RNA-seq (n = 22) analyses confirmed that *C19MC* was recurrently targeted by amplification/copy-number gains and fusions with *TTYH1* (Figure 1C). Consistently, profiling of 565 miRNAs using NanoString analyses (Figure 1D; Table S1) showed that *C19MC* oncomiRs, and not the syntenic miR371-373 cluster (Li et al., 2009), were exclusively upregulated in ETMRs, while expression of miR-15 and the let-7 tumor suppressor miRNAs were downregulated in ETMRs relative to other PBTs. Interestingly, the embryonic stem cell (ESC)-enriched 17–92 oncomiR cluster implicated in medulloblastoma (Murphy et al., 2013), was upregulated in other PBTs, but only modestly expressed in ETMRs, underscoring a very specific causative role for *C19MC* oncomiRs in ETMRs.

C19MC oncomiRs Cooperatively Target Multiple Cell-Cycle Tumor Suppressors

We previously showed that individual *C19MC* miRNAs, miR520g and miR517c, can promote *in vitro* and *in vivo* transformation (Li et al., 2009); however, the collective effect of *C19MC* oncomiRs and the nature of common *C19MC* target genes in ETMRs have not been examined. To elucidate *C19MC* oncogenic mechanisms, we investigated the effect of a maxi-gene containing five *C19MC* miRNAs (5miR) (Figures S2A and S2B) most highly expressed in primary ETMRs (Li et al., 2009), on growth of A664—a cell line derived from a primary ETMR (Figures S2C–S2F) and hNSC6, an hNSC line. Stable 5miR expression enhanced both A664 and hNSC6 cell viability and accelerated G1/S transition in hNSC6, while miR520g expression had limited effects on hNSC6 growth (Figures 2A and 2B). These observations indicated that multiple *C19MC* oncomiRs may act cooperatively on gene targets to promote ETMR transformation.

To identify *C19MC* oncomiR targets relevant to primary ETMR biology, we first performed comparative RNA-seq analyses of hNSC6-5miR and corresponding vector controls to identify *C19MC* responsive genes and then integrated these data with differential RNA-seq analyses of ETMRs versus other PBTs to identify *C19MC* targets or effectors specifically enriched in ETMRs (detailed in Table S2). Differential analyses of hNSC6-5miRs versus control lines revealed 12,729 *C19MC* responsive genes (6,305 up- and 6,424 downregulated genes; n = 2; false discovery rate [FDR] < 0.05; fold change [FC] > 1.2, <−1.2), while analyses of primary ETMRs (n = 22) and other PBTs (n = 17) revealed 6,002 enriched genes (FDR < 0.05; FC > 1.2, <−1.2). Integration of the two datasets identified 4,192 common genes, of which 2,044 and 2,148 were, respectively, up- and downregulated in both hNSC6-5miR cells and ETMRs. Functional enrichment analyses of the 4,192 *C19MC* responsive genes revealed neural stem cell maintenance, epigenetic regulation, and miRNA processing genes as *C19MC* upregulated targets, while apoptosis, mRNA stability, and neurogenesis genes comprised *C19MC* downregulated targets (Figures 2C and 2D; Table S2).

In keeping with the rapidly proliferative nature of ETMRs and accelerated cell-cycle phenotypes in hNSC6-5miR cells, genes involved in cell-cycle regulation comprised one of the largest *C19MC* responsive hubs (12.5%; $p = 1.32 \times 10^{-22}$; 347 up- and 179 downregulated genes). As miRNAs predominantly negatively regulate gene expression, we focused on the 3′ UTR sequences of the 179 downregulated cycle-cell genes to identify *C19MC* binding sites, using strict criteria detailed in methods. These analyses revealed that only 11/179 *C19MC* downregulated genes harbored multiple evolutionarily conserved *C19MC* miRNA binding sites in their 3′ UTRs (Table S2). We applied H3K27Ac chromatin immunoprecipitation sequencing (ChIP-seq) and assay for transposase-accessible chromatin using sequencing (ATAC-seq) data available for 5 ETMRs to assess the functional status of these loci in primary tumors and observed that only 5/11 loci, including *AHR*, *CCND2*, *CDKN1A* (p21), *CDKN1B* (p27), and *RBL2*, exhibited both active enhancer marks and open chromatin in a majority (>3/5) of ETMRs (Table S2). Our analyses did not identify *MYC* or *MAX*, pRB pathway tumor suppressor genes (*CDKN2A/B*, *CDKN2C*, and *RB1*), *TP53* or *PTEN*, which are frequently implicated in other brain tumors,

(F) Summary of luciferase reporter assays in UW228 cells co-transfected with combinations of empty vector or miR520g/5miR expression plasmids, and wild-type (WT), mutated p21, or p27 3′ UTR reporter constructs; 3′ UTR 520g-t constructs served as miRNA target binding control. Luciferase activity was normalized to Renilla and vector control.

(G) High-magnification image of miRNA *in situ* hybridization (ISH) and immuno-histochemical (IHC) analyses performed on sequential tissue sections of primary ETMR using fluorescence-labeled miR520g and scrambled control (scr) probes, and anti-p21, p27, and RBL2 antibodies. Scale bars, 100 μm. miRNA expression and tumor nuclei are respectively visualized in green and blue; corresponding regions in inset lower-magnification images are indicated by arrows. Scale bars, 20 μm.

Ctrl indicates controls; data are presented as means ± SEM (n = 3); significance was determined by unpaired two-tailed Student's t test; *p < 0.05; mRNA expression is normalized to actin and tubulin served as western blot loading controls.

See also Figure S2 and Table S2.

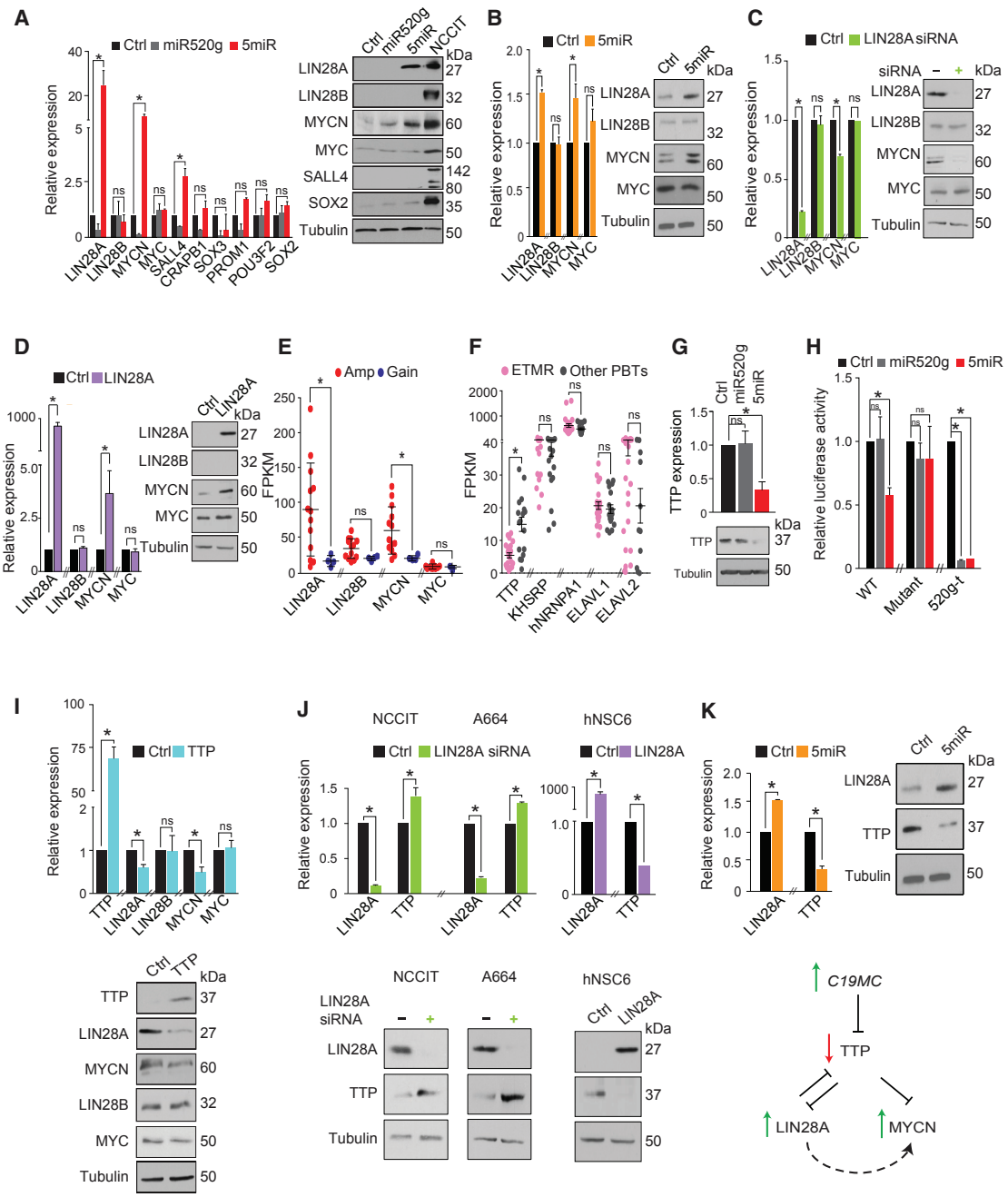

Figure 3. *C19MC*-LIN28A-MYCN Comprise an Oncogenic Circuit

(A) qRT-PCR and western blot analyses of predicted *C19MC* targets and other neural developmental genes in stable hNSC6-miR520g, hNSC6-5miR, and control cell lines. NCCIT lysates served as antibody control.

(B and C) qRT-PCR and western blot analyses of A664-5miR (B) or vector control cell lines (C) transfected with LIN28A or control siRNA.

(D) qRT-PCR and western blot analyses of hNSC6-LIN28A or vector control lines.

(E) RNA-seq FPKM expression values for LIN28A/B and MYC/N in ETMRs with *C19MC* amplification (n = 13) or copy-number gains (n = 4); *q < 0.05. Data are presented as individual samples, with means ± SEM indicated.

(F) RNA-seq FPKM expression values for RNA-binding proteins predicted to target *LIN28A* and *MYCN* 3′ UTR in ETMR (n = 22) and other PBTs (n = 17); *q < 0.05. Data are presented as individual samples, with means ± SEM indicated.

(G) qRT-PCR and western blot analyses of hNSC6-miR520g, hNSC6-5miR, and control cell lines.

(H) Summary of luciferase reporter assays in UW228 cells co-transfected with empty vector, miR520g, 5miR expression constructs, and reporter constructs of wild-type (WT) or TTP 3′ UTR with mutant *C19MC* binding sites; 520g-t constructs served as miRNA target binding control. Luciferase activity is normalized to Renilla and vector control.

(I) qRT-PCR and western blot analysis of A664 cells transfected with control or TTP expression construct.

(legend continued on next page)

as *C19MC* targets. Notably, *CDKN2A/2B*, which were significantly downregulated in ETMRs (Figure 2C), lacked H3K27Ac marks and/or open chromatin in a majority of tumors, indicating that they were predominantly transcriptionally regulated.

As AHR and CCND2 have variably reported tumor suppressor activity, we focused on validating canonical cell-cycle tumor suppressors p21, p27, and RBL2 as direct *C19MC* targets (Figure S2G). Consistent with cooperative effects of *C19MC* oncomiRs on gene targets, p21, p27, and RBL2 mRNA and protein were diminished by up to 2-fold in stable A664 and hNSC6 cell lines expressing 5miRs versus miR520g, and *C19MC*-mediated repression was conserved across different brain tumor cell lines (Daoy, UW228, PFSK) (Figures 2E and S2H–S2J). Importantly, expression of p14/16, RB1, TP53, and PTEN were unchanged in response to 5miR and anti-miR-mediated targeting of endogenous *C19MC* 5 miRs in ETMR2373—a *C19MC* amplified cell line, also rescued expressions of p21, p27, and RBL2, without effects on other cell-cycle regulators (Figures S2E, S2F, and S2K). Direct gene targeting by *C19MC* was confirmed using 3′ UTR luciferase promoter assays, which showed that 5miR mediated significantly greater inhibition of p21 and p27 3′ UTR activity than miR520g in UW228 cells, while repressive effects of both miR520g and 5miR were abrogated by mutations to *C19MC* binding sites on p21 and p27 3′ UTRs (Figures 2F and S2L). Immuno-histochemical and miRNA *in situ* hybridization analyses confirmed that p21, p27, and RBL2 protein were absent in tumor cells with high *C19MC* oncomiR expression (Figure 2G), thus confirming these multiple cell-cycle tumor suppressors as relevant and direct targets of *C19MC* oncomiRs in primary ETMRs.

C19MC-LIN28A-MYCN Comprise a Feedforward Oncogenic Circuit

As ETMRs exhibit few other regions of focal copy-number alterations, we reasoned that *C19MC* may also drive ETMR growth via upregulation of oncogenes. Indeed, multiple oncogenes with functions in stem cell maintenance and neurogenesis were represented in the top 1% of the 2,044 genes (FDR = 7.58×10^{-5}) commonly upregulated in hNSC6-5miR and ETMRs (Figures 2C and 2D). H3K27Ac ChIP-seq and ATAC-seq analyses revealed that 17 of the top 20 enriched genes, which included *MYCN* and *LIN28A*, exhibited active enhancer markers and open chromatin in a majority (3–5) of primary ETMRs (Table S2). Western blot and qRT-PCR analyses showed that MYCN and LIN28A, but not the closely related MYC and LIN28B loci, were upregulated in hNSC6-5miR, while only MYCN was upregulated in hNSC6-miR520g cells (Figures 3A and S3A). Other genes enriched in ETMRs, including *SALL4*, *CRABP1*, *SOX2/3*, *PROM1*, and *POU3F2*, showed inconsistent or no changes with 5miR or miR520g expression. These findings, which suggested that MYCN and LIN28A were specific targets of *C19MC*, was further confirmed by analyses of stable A664-5miR cell lines (Figures 3B and S3A). As reciprocal LIN28B and MYCN regulation is observed in neuroblastoma, a pediatric peripheral nervous system tumor (Powers et al., 2016), we investigated the possibility of a *C19MC*-LIN28A-MYCN regulatory circuit. Indeed, LIN28A knockdown in A664 and LIN28A expression in hNSC6 cells respectively resulted in up- and downregulation of MYCN, while MYC was unchanged (Figures 3C, 3D, and S3A). Notably, we also observed that LIN28A and MYCN, but not LIN28B and MYC levels, correlated quantitatively with *C19MC* copy-number gains and amplification in primary tumors (Figure 3E), indicating that *C19MC* oncomiRs act cooperatively and specifically to drive the LIN28A-MYCN regulatory loop in ETMR.

To investigate *C19MC*-mediated regulation of LIN28A and MYCN, we examined the 3′ UTRs of both oncogenes for potential target sequences of AU-rich element RNA-binding proteins (ARE-RBP), which function in mRNA decay. These analyses revealed 24 and 31 candidate ARE-RBPs, respectively, for LIN28A and MYCN; 3 of 5 ARE-RBPs predicted to target both oncogenes (TTP, KHSRP, hnRNPA1, and ELAVL1/2) harbored *C19MC* binding sites at 3′ UTRs (Figures S3B and S3C; Table S3). Of these, only TTP (Tristetraprolin) was significantly downregulated in ETMR relative to other PBTs (Figure 3F), indicating that *C19MC* may act via TTP repression to upregulate LIN28A and MYCN. Indeed, stable 5miR expression robustly downregulated TTP in hNSC6 cells (Figures 3G and S3D), while mutation of *C19MC* binding sites on TTP 3′ UTR rescued 5miR-mediated repression of TTP in luciferase reporter assays (Figures 3H and S3E). Furthermore, transient TTP expression in A664 cells led to diminished LIN28A and MYCN, but not LIN28B and MYC expression (Figures 3I and S3D). Interestingly, we observed that TTP was also upregulated with LIN28A knockdown in A664 as well as NCCIT, a germ cell tumor line with high endogenous LIN28A, and diminished in stable hNSC6-LIN28A cell lines, thus indicating that TTP also maps downstream of LIN28A. Consistently, TTP was downregulated in A664-5miR cells, which have high LIN28A expression (Figures 3J, 3K, and S3D). Our aggregate findings suggest that multiple feedback loops drive a *C19MC*-LIN28A-MYCN oncogenic circuit in ETMRs.

LIN28A Modulates Epigenetic Effectors in ETMRs

The discovery of a *C19MC*-LIN28A-MYCN circuit together with high LIN28A expression in ETMRs implies a significant oncogenic role for LIN28A. Indeed, we observed that LIN28A expression and knockdown, respectively, enhanced and diminished viability of hNSC6 and A664 cells (Figures 4A and 4B). To investigate LIN28A oncogenic mechanisms and map ETMR-specific LIN28A targets, we performed and compared RNA-immunoprecipitation (RIP) coupled with RNA-seq analysis of A664 cells with RNA-seq profiles of A664 and primary ETMRs. Consistent with LIN28A functions in mRNA binding and stabilization (Wilbert et al., 2012), the largest category of LIN28A targets (49.4%) mapped to exonic and 3′ UTR sequences (Figure S4A). RIP

(J) qRT-PCR and western blot analysis of NCCIT, A664 cells treated with LIN28A, or control siRNA and hNSC6-LIN28A stable cell lines.
(K) qRT-PCR and western blot analysis of stable A664-5miR and control cell lines. Schema shows *C19MC*-mediated regulation of LIN28A/MYCN via TTP inhibition. Validated and predicted regulation are shown by solid and dashed lines, respectively.
In all cell line experiments, Ctrl indicates controls, data are presented as means ± SEM (n = 3); significance was determined by unpaired two-tailed Student's t test; *$p < 0.05$; mRNA expression is normalized to actin and tubulin served as western blot loading controls.
See also Figure S3 and Table S3.

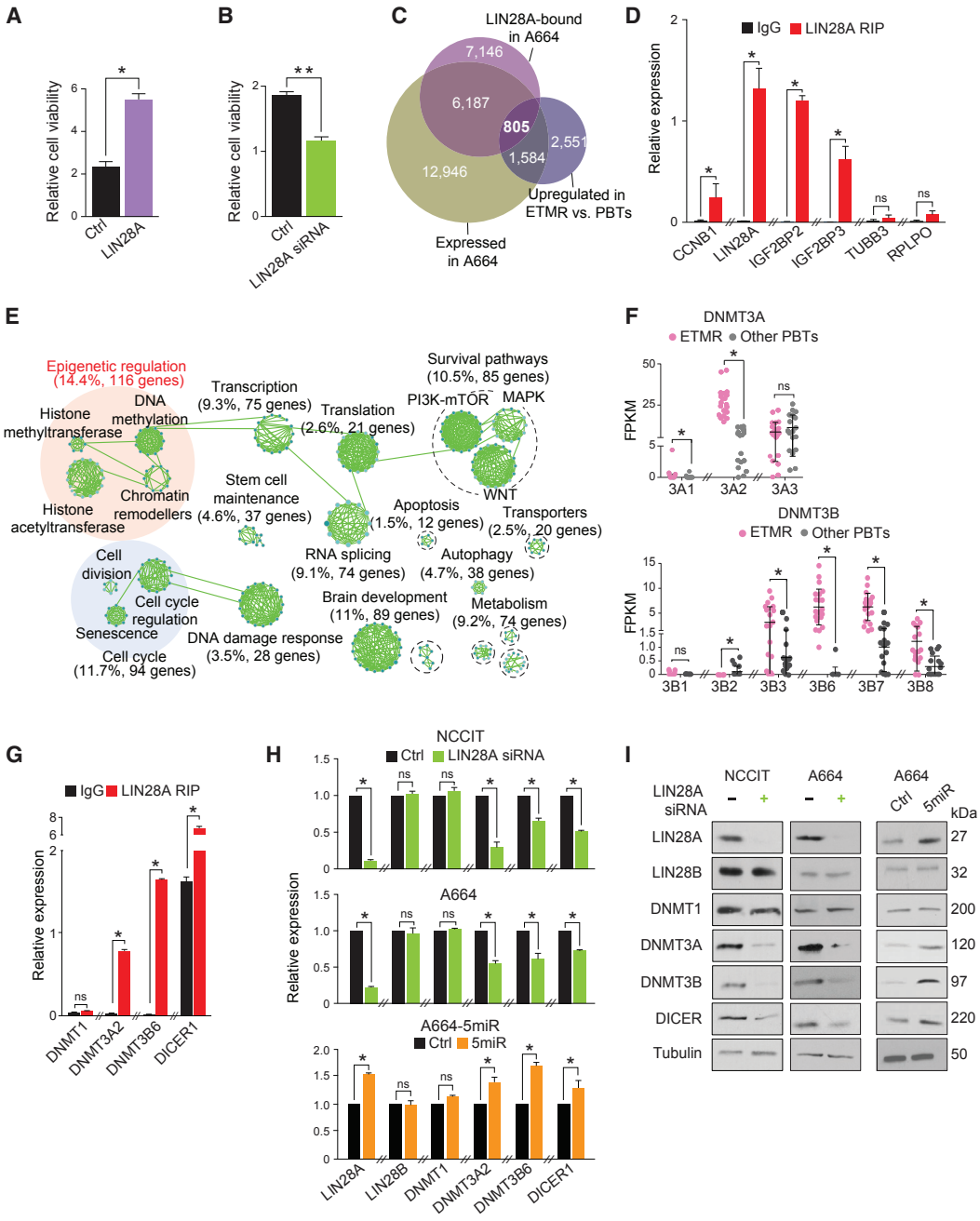

Figure 4. LIN28A Modulates Epigenetic Effectors in ETMR

(A) Cell viability assays for stable hNSC6-LIN28A and corresponding vector control cell lines.

(B) Cell viability assays for A664 cell line treated with LIN28A or control siRNA.

(C) Schema for LIN28A target identification in RIP analyses of A664 cells. Green and purple circles, respectively, correspond to all genes expressed in A664 cells (FPKM > 1) and unique LIN28A-bound genes in A664 cells; blue circle corresponds to all genes significantly upregulated in ETMRs versus PBTs ($q < 0.05$).

(D) qRT-PCR validation analyses of A664 LIN28A RIP and control immunoglobulin G (IgG) IP samples for known LIN28A targets and non-enriched genes; data are normalized to RIP input control.

(E) Cystoscape visualization of gene set enrichment analysis of 805 LIN28A-bound genes. Percentage and number of genes in each biological process are shown.

(F) RNA-seq FPKM values for DNMT3A and DNMT3B isoforms in primary ETMR (n = 22) and other PBTs (n = 17); *$q < 0.05$. Data are presented as individual samples, with means ± SEM indicated.

(G) qRT-PCR analysis of A664 RIP and control IgG IP samples. Data are normalized to input control.

(legend continued on next page)

sequencing analyses identified 38,405 LIN28A binding sites (>2-fold enrichment; $p < 0.05$) corresponding to 7,146 unique target genes of which 805 were commonly enriched in A664 cells and ETMRs (Figure 4C). Specificity of LIN28A RIP was confirmed by qRT-PCR analyses of known LIN28A targets (*CCNB1*, *LIN28A*, and *IGF2BP2/3*) (Peng et al., 2011; Wilbert et al., 2012), and unrelated genes (*TUBB3* and *RPLPO*) (Figure 4D). Consistent with our previous work, functional enrichment analyses showed a substantial proportion of LIN28A targets mapped to cell growth, survival, and metabolism pathways (Figure 4E; Table S4). Strikingly, epigenetic regulators including miRNA processing gene, *DICER1* and *de novo* DNA methyltransferases (*DNMT3A/3B*), which exist in multiple isoforms during embryonic and fetal development, comprised the largest category (14.4%; 116/805 genes) of LIN28A-regulated transcripts enriched in ETMRs (Figure S4B). Although, LIN28A binding sites mapped to common 3′ UTRs of *DNMT3A* and *DNMT3B* invariant exons 16/17, RNA-seq analyses indicated that *DNMT3A2* and the enzymatically active *DNMT3B6* isoform were most highly enriched in ETMRs relative to other PBTs (Figures 4F and S4C–S4E). Consistently, RIP qRT-PCR analyses showed LIN28A binding and enrichment of *DICER1*, *DNMT3A2*, and *DNMT3B6*, but not *DNMT1,* in A664 cells (Figure 4G), and that LIN28A knockdown diminished DNMT3A2, DNMT3B6, and DICER1 mRNA and protein expression, but had no effects on LIN28B and DNMT1 in A664 and NCCIT cells. Significantly, while DNMT3A2/3B6 and DICER1 mRNA and protein were also specifically upregulated in A664-5miR cells (Figures 4H, 4I, and S4F), treatment of ETMR2373 with anti-miRs targeting five *C19MC* miRs only resulted in downregulation of MYCN, LIN28A, and DNMT3A2/3B6 (Figure S4G). These collective findings suggest that the *C19MC*-LIN28A-MYCN oncogenic circuit acts in concert to enhance *C19MC* oncomiRs and embryonic DNMT3A2/B6 expression, and thus plays a critical role in promoting or maintaining the primitive, malignant epigenetic state that characterize ETMRs (Kleinman et al., 2014).

Hijacked Super-Enhancers Amplify the *C19MC*-LIN28A-MYCN Oncogenic Circuit

As enhancer hijacking by genomic alterations is increasingly implicated as an important mechanism in cancers (Lin et al., 2016; Northcott et al., 2014), we asked whether similar mechanisms may contribute to the *C19MC*-LIN28A-MYCN oncogenic circuit in ETMRs. To investigate these possibilities, we performed and integrated H3K27Ac ChIP-seq (nine tumors) and ATAC-seq (seven tumors) with copy-number and RNA-seq analyses of primary ETMRs to identify *C19MC*-, MYCN-, or LIN28A-associated enhancers that may be co-opted by genomic alterations. In addition, we used C3D (cross cell-type correlation) analysis, a tool to predict *cis*-regulatory interactions, on ETMR ATAC-seq data to determine whether these loci may be targeted by long-range DNA-DNA interactions.

Although previous limited RNA-seq studies suggested that high *C19MC* expression was driven by fusion of *TTYH1* promoter and *C19MC* gene body, more detailed mapping of RNA-seq data from a larger cohort of 22 ETMRs revealed greater complexity to the *TTYH1-C19MC* fusion events (Table S5). Significantly, our analyses showed that *TTYH1-C19MC* fusion breakpoints flanked a broad genomic area of ~790 kbs (Chr19: 54,142,428–54,932,953 bp) enriched for H3K4me1, H3K27me3, and H3K27ac marks and DNase I hypersensitive sites, indicating that *TTYH1-C19MC* gene fusions may juxtapose distinct putative *TTYH1*- and *C19MC*-associated enhancers to generate a unique hybrid super-enhancer (Figure 5A). H3K27Ac ChIP and ATAC-seq analyses of ETMRs confirmed that *TTYH1-C19MC* fusion breakpoints flanked a large chromatin accessible region that included a *C19MC*-associated enhancer element (Chr19: 54,162,824–54,167,441) ~7 kb upstream of the first *C19MC* miRNA (*miR-512-1*) and 20.3 kb downstream of the genomic breakpoint (Chr19: 54,142,428), and a *TTYH1*-associated enhancer region (Chr19: 54,925,236–54,933,011) spanning a 7.7-kb region enriched for multiple transcription factor (TF) binding sites, indicating that it was a super-enhancer (Filippova et al., 1996; Malik et al., 2014) (Figures 5B and S5). Significantly, C3D analysis of ETMR ATAC-seq data revealed high probability ($r = 0.84$; $p = 2.63 \times 10^{-10}$) of direct and specific interaction between the *C19MC* and *TTYH1* super-enhancer regions (Figure 5C; Table S5) and low probability of DNA-DNA interactions between flanking regions Chr19: 54,929,312–54,930,435 and Chr19: 54,960,066–54,960,945. Collectively these findings point to a unique hybrid super-enhancer, created by the *TTYH1-C19MC* gene fusion (Figure 5D) that spans 32.73 kb, as a major driver of high *C19MC* oncomiR expression in ETMRs. Notably, the *TTYH1-C19MC* hybrid super-enhancer region exhibited multiple TF binding sites for MYC and MYC-binding partners, MAX and MAZ, further underscoring the importance of MYCN and a reciprocal *C19MC*-MYCN feedforward regulatory circuit in ETMRs.

In contrast, detailed SNP, methylation, and RNA-seq analyses did not reveal any focal *LIN28A* or *MYCN* genomic alterations in ETMRs. C3D analyses of ATAC-seq data predicted no significant DNA-DNA interactions targeting the *LIN28A* promoter in ETMRs. However, C3D/ATAC-seq analyses of ETMRs revealed a high probability of long-range interactions between the *MYCN* promoter (Chr2: 16,079,544–16,080,544) and five chromatin accessible regions on Chr2 (Chr2: 16,124,310–16,124,602, 16,154,035–16,154,821, 16,397,969–16,398,207, 16,404,397–16,405,254, 16,511,152–16,512,136; $r > 0.8$; $p < 1 \times 10^{-10}$) within 1.5 Mb upstream of *MYCN* (Figure 6A; Table S6). ChIP-seq analyses of ETMRs showed that all five regions were enriched for H3K27Ac marks and spanned binding sites for multiple TFs, including CTCF, MYC, and MAX, indicating that they represented five distinct enhancers (e1–e5) (Figures 6B and S6A). Notably enhancers e1–e5, which correlated with high *MYCN* expression were only evident in ETMRs and hNSCs derived from 11-week-old fetal brain. These findings suggest that distinct long-range interactions between the *MYCN* promoter and early embryonic restricted e1–e5 enhancers contribute to the *C19MC*-LIN28A-MYCN oncogenic circuit.

(H and I) qRT-PCR (H) and western blot analysis (I) of NCCIT and A664 cells treated with LIN28A or control siRNA, and in stable A664-5miR and vector control cell lines. In all cell line experiments, controls are indicated by Ctrl, data are presented as means ± SEM (n = 3); significance was determined by unpaired two-tailed Student's t test; *$p < 0.05$, **$p < 0.01$; mRNA expression is normalized to actin and tubulin served as western blot loading controls.
See also Figure S4 and Table S4.

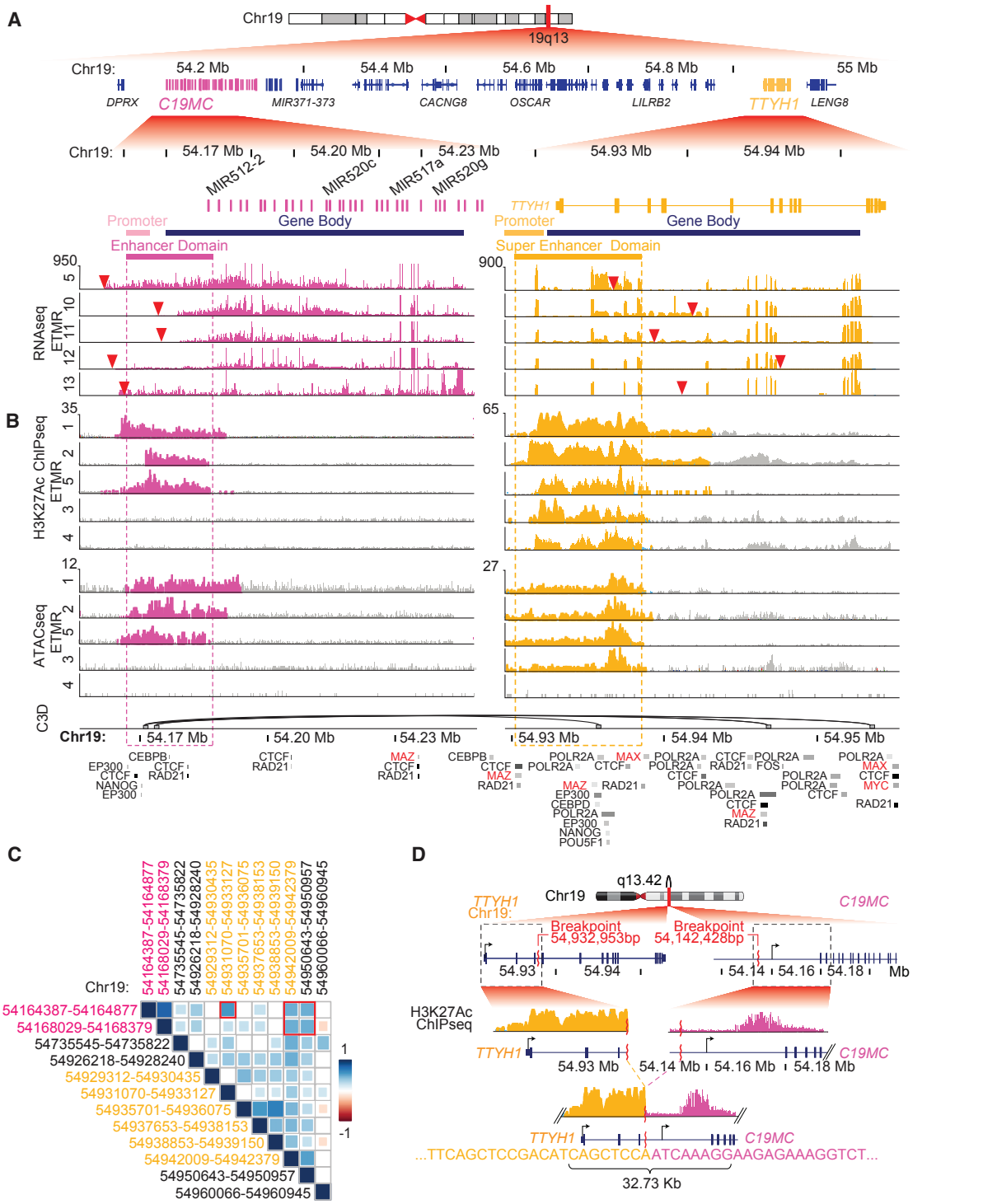

Figure 5. A Hybrid Super-Enhancer Is Generated by *C19MC-TTYH1* Gene Fusion

(A) Schematic map of Chr19q13.42 with zoomed view of *C19MC* (Chr19: 54,144,653–54,271,357) and *TTYH1* (Chr19: 54,924,605–54,949,899) relative to UCSC hg19 RefSeq annotation and ENCODE tracks. *TTYH1-C19MC* fusion breakpoints (red inverted arrows) aligned to RNA-seq reads in five representatives primary ETMRs are shown in relation to *C19MC* and *TTYH1* promoter, predicted enhancers/super-enhancer (dashed boxes) and gene bodies.

(B) H3K27Ac ChIP-seq and ATAC-seq tracks from ETMR with (n = 3) and without (n = 2) *C19MC* amplification, is aligned relative to UCSC gene tracks and ENCODE predicted *C19MC* enhancer (pink) and *TTYH1* super-enhancer (orange) regions (dashed boxes). DNA-DNA interactions predicted by ATAC-seq/C3D analyses of primary ETMR—see (C)—are indicated by curved lines and shown relative to ENCODE ChIP-seq map of transcription factor binding sites; MYC/MAZ binding sites are highlighted in red.

(legend continued on next page)

Interestingly, consistent with RNA-seq analyses of ETMRs and hNSCs (Figure 6C), a comparison of H3K27Ac enrichment patterns in ETMRs and hNSCs using the ENCODE/Epigenomic Roadmap database showed coordinated *TTYH1*, *C19MC*, *LIN28A*, *MYCN*, and *DNMT3B6* active enhancer patterns only in ETMRs and 11-week-old fetal brain-derived hNSCs, and only partial overlap with enhancer patterns in other hNSCs and human placenta (Figures 6D and S6B). In contrast to *DNMT3B6*, the *DNMT3A2* enhancer was present in a broader spectrum of normal and cancer cells. While ETMRs with *C19MC* alterations exhibited both the *TTYH1*- and *C19MC*-associated enhancers, only *TTYH1*-associated enhancers were evident in ETMRs without *C19MC* alterations. Taken together, our data suggest that unique *TTYH1-C19MC* hybrid super-enhancers and long-range *MYCN*-enhancer interactions amplify a *C19MC*-LIN28A-MYCN oncogenic circuit and drives expression of embryonic restricted DNMT3B6 to promote a primitive malignant epigenetic state in ETMRs.

An MYCN-Dependent Core Regulatory Circuit Represents a Therapeutic Vulnerability in ETMRs

Our collective analyses suggest that MYCN dysregulation is a critical component of the *C19MC*-driven oncogenic circuit in ETMRs. As MYC has been implicated as a master TF, which drives super-enhancer-dependent regulatory circuits and therapeutic vulnerabilities in cancer cells (Schuijers et al., 2018; Zeid et al., 2018), we investigated if MYCN may act similarly in ETMRs. We applied the ROSE algorithm (Loven et al., 2013; Whyte et al., 2013) on H3K27Ac ChIP-seq data from 5 primary tumors and identified 1,330 super-enhancers, which were then subjected to a core regulatory circuitry (CRC) analysis to identify key TFs that drive auto-regulatory loops (Saint-Andre et al., 2016). Of 190 candidate TFs (Table S7), 18 emerged as core TFs that mapped to open chromatin regions, were highly expressed (fragments per kilobase million > 20) in ETMRs, and upregulated in hNSC6-5miR cells (Figure S7A). These included MYCN and known MYC-binding partner, MAZ (Figure 7A). Notably, gene set enrichment analyses of the global super-enhancer functional network in ETMRs confirmed a predominance of MYCN/MAZ-regulated processes including embryonic and CNS development, cellular metabolism, differentiation, and survival (Figure 7B; Table S7), which are prominent features of ETMR transcriptional signatures (Li et al., 2009). Consistent with these analyses, *MYCN* and *MAZ* expression were significantly higher than that of *MYC* and its canonical partner *MAX*, in ETMRs and during early brain development, as indicated by BrainSpan data (Figures 7C and 7D). These findings suggest that the *C19MC*-LIN28A oncogenic axis critically drives ETMR cell growth primarily via an MYCN/MAZ-mediated core transcriptional regulatory circuitry. To investigate this possibility, we treated A664 parental, A664-vector controls, and A664-5miR stable cell lines with JQ1S, an active isomer of JQ1, a bromodomain inhibitor that selectively inhibits super-enhancer-associated oncogenes such as MYC/MYCN. A664-5miR cells exhibited greatest sensitivity to JQ1S, with up to 50% dose-dependent reduction in cell viability as compared with parental or vector control cells (Figures 7E and S7B). Notably, qRT-PCR and western blot analyses of cells treated with JQ1S and control inactive isomer JQ1R showed significantly greater downregulation of *C19MC* responsive core regulatory circuit effectors MYCN, MAZ, LIN28A, DNMT3B6/A2, and BRD2, in JQ1S-treated A664-5miR cells as compared with controls (Figures 7F, S7C, and S7D). JQ1S treatment in ETMR2373 cells also robustly diminished expression of endogenous *C19MC* miRNAs, LIN28A and DNMT3B6, concomitant with increased PARP cleavage, without effects on LIN28B, DNMT1, and DNMT3A2 mRNA and protein expression (Figures 7G and S7E). These findings suggest that convergence of the *C19MC*-LIN28A and MYCN oncogenic circuits critically drive ETMR cell growth and represent a distinct therapeutic vulnerability in ETMRs (Figure 8).

DISCUSSION

C19MC oncomiRs are upregulated in a spectrum of cancers (Huang et al., 2008; Rajaram et al., 2007; Rippe et al., 2010), but oncogenic genomic alterations are rare in most cancers. In contrast, our analyses revealed that a majority of ETMRs exhibit *C19MC* amplifications/gene fusions and few other recurrent CNAs, underscoring *C19MC* as a specific and major oncogenic driver in this disease. Indeed, our cumulative data suggest that *C19MC* is a powerful oncogene that acts to modulate tumor suppressors and oncogenes in ETMRs. We show that *C19MC* oncomiRs cooperatively target multiple cell-cycle regulators to promote proliferation in hNSC and ETMR cells in a manner similar to the orthologous murine miR290–295 cluster that inhibits ESC-cycle exit by targeting multiple checkpoint genes (Lichner et al., 2011; Wang et al., 2014). Notably, our data show that *C19MC* acts via inhibition of TTP, an ARE binding tumor suppressor protein, to specifically upregulate the oncogenes LIN28A and MYCN, but not MYC, which is regulated by TTP in other cancers (Kim et al., 2012; Lee et al., 2013). Interestingly, our data show that LIN28A also acts as a negative and positive regulator for TTP and MYCN, respectively, thus indicating a *C19MC*-LIN28A-MYCN oncogenic circuit that is driven by multiple convergent mechanisms in ETMRs. Although ETMRs also have high LIN28B expression, our studies show the *C19MC*/TTP axis only targets LIN28A, indicating that LIN28B is regulated by alternate mechanisms. Consistent with our previous studies that implicated a LIN28A-let-7 axis in ETMR cell growth (Spence et al., 2014a, 2014b), we observed very limited expression of let-7 in ETMRs. Whether let-7 contributes to LIN28A-MYCN

(C) Composite correlation matrix of associated open chromatin regions in a 1.5-Mb window around the *C19MC* enhancer predicted by C3D analysis of ATAC-seq data from five ETMRs. Absolute correlation is shown proportional to size of colored square, positive and negative correlations are indicated in blue and red, respectively. Red box indicates statistically significant areas. All correlations were adjusted for statistical significance ($p < 10 \times 10^{-10}$); blank squares indicate insignificant correlations.

(D) Schema of a representative tumor (ETMR5) showing alignment of *TTYH1:C19MC* fusion breakpoints (red) with corresponding H3K27Ac ChIP-seq peaks and resulting hybrid *TTYH1* and *C19MC* super-enhancer. *TTYH1* and *C19MC* transcriptional start sites are shown in relation to the sequence of a 32.7-kb hybrid enhancer.

See also Figure S5 and Table S5.

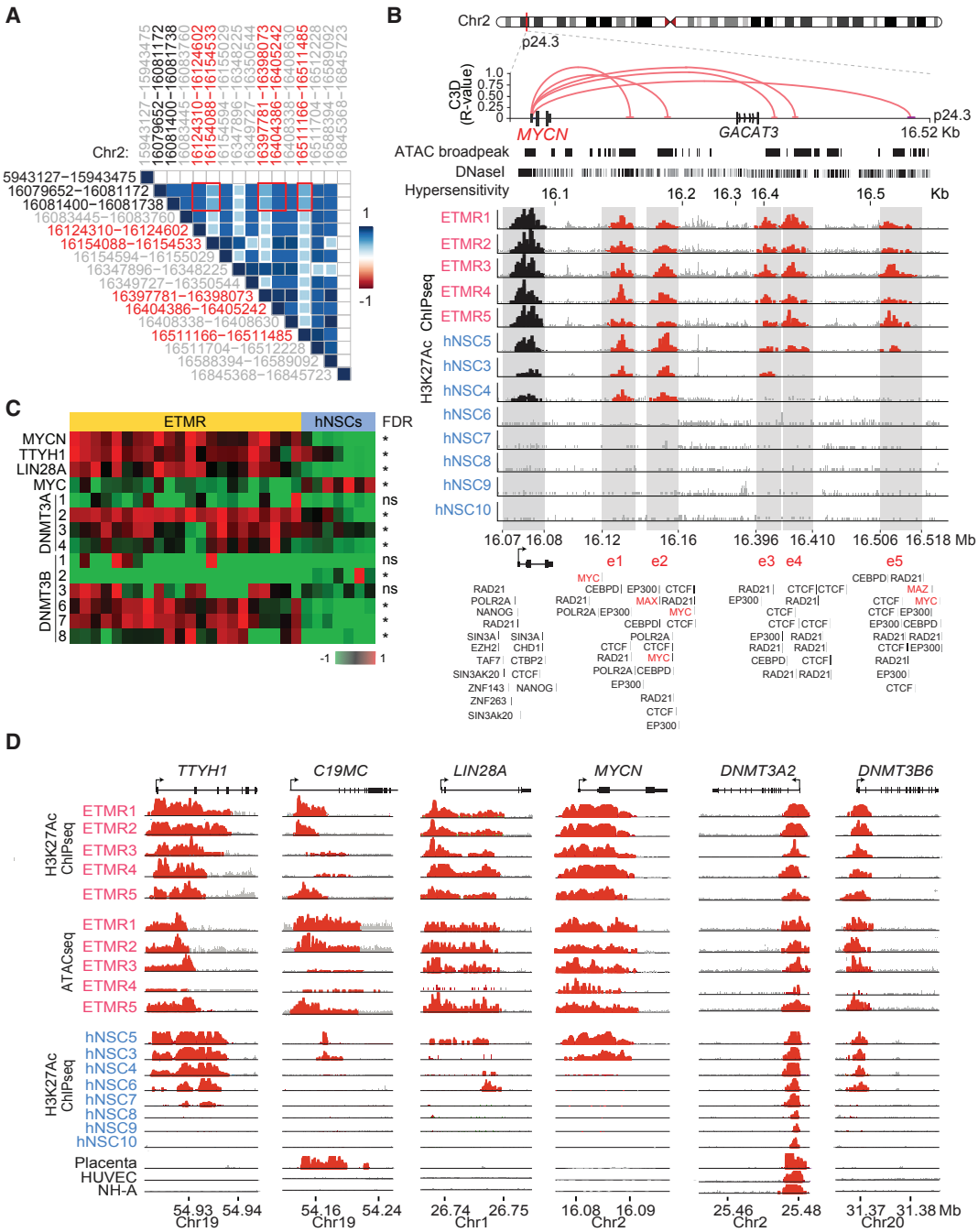

Figure 6. *MYCN* Is Targeted by Long-Range Enhancer Interactions on Chr2

(A) Composite correlation matrix of associated open chromatin regions of the *MYCN* promoter and distal Chr2 regions predicted by C3D/ATAC-seq analysis of five ETMRs. Absolute correlation is shown proportional to size of colored squares, positive and negative correlations are indicated in blue and red, respectively. Red boxes mark statistically significant areas. All correlations were adjusted for statistical significance ($p < 10 \times 10^{-10}$); blank squares indicate insignificant correlations.

(B) Zoomed view of a 439-kb putative MYCN promoter-super-enhancer region mapped using H3K27Ac ChIP and C3D/ATAC-seq analyses of primary ETMRs and hNSCs. Arcs indicate predicted interactions of *MYCN* promoter and five distal enhancers (e1–e5); arc height corresponds to average probability of interactions (R value). Composite ATAC-seq maps from five ETMRs are shown in relation to ENCODE DNase I hypersensitivity map. H3K27Ac marks at e1–e5 in ETMRs and hNSC cell lines are shown relative to ENCODE TF ChIP-seq data; predicted MYC-binding sites are highlighted in red.

(C) Gene expression heatmap showing *MYCN*, *TTYH1*, *LIN28A*, *MYC*, and *DNMT3A2/3B6* isoform levels in ETMRs (n = 22) and hNSCs (n = 7) determined by RNA-seq; *q < 0.05.

(D) IGV alignment tracks for indicated genes from H3K27Ac ChIP-seq and ATAC-seq analyses of five ETMRs and eight hNSC lines are shown relative to ENCODE/Epigenomic Roadmap H3K27Ac ChIP-seq datasets for placenta, human umbilical vein endothelial cells (HUVEC), and normal human astrocytes (NH-A).

See also Figure S6 and Table S6.

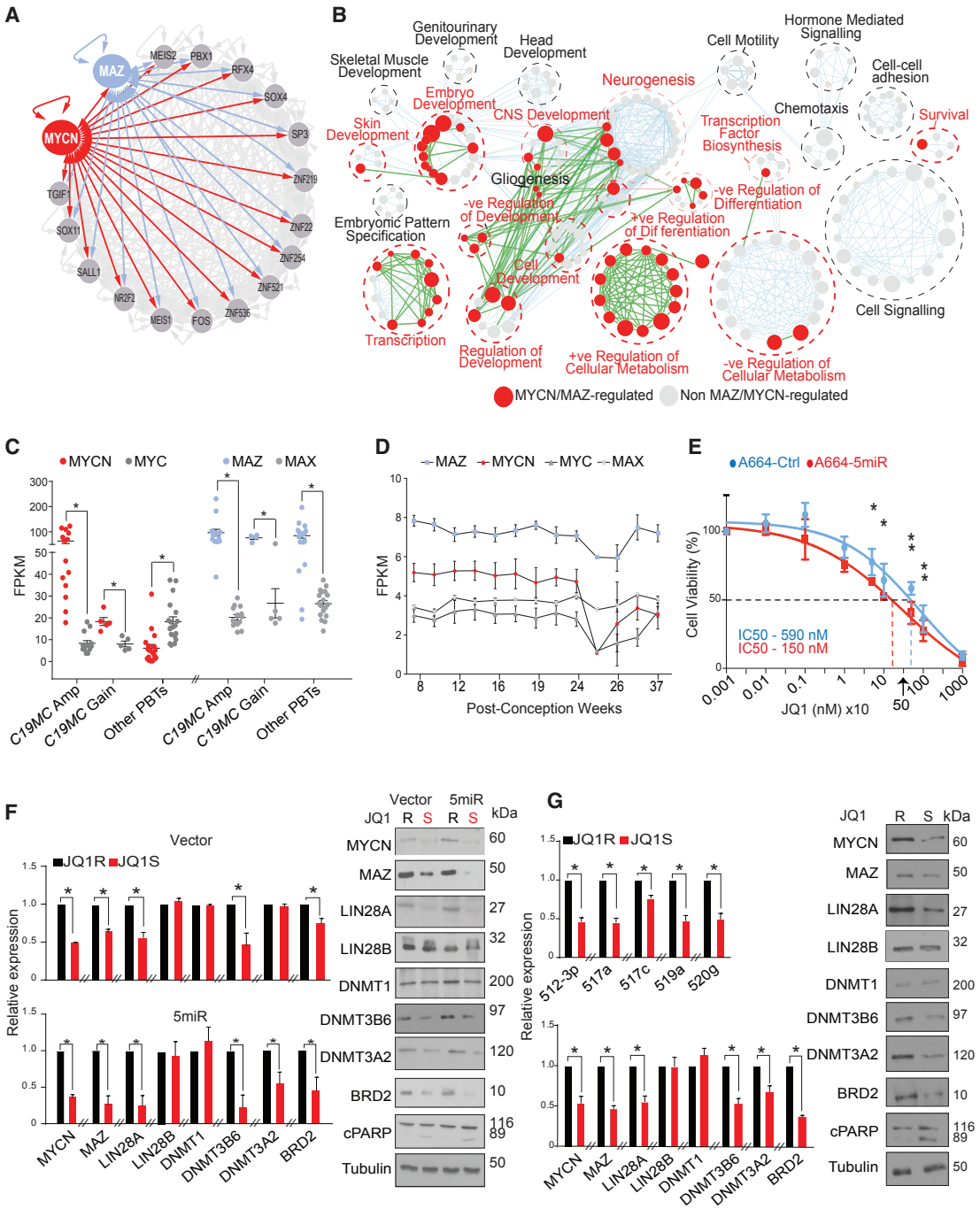

Figure 7. MYCN Drives a Super-Enhancer-Mediated Core Regulatory Circuit in ETMRs

(A) Diagram of MYCN/MAZ-mediated transcriptional regulatory network and 18 interacting super-enhancer transcription factors (gray circles) identified using enhancer-based core regulatory analysis (CRC) of 5 ETMRs. Relationship to MYCN or MAZ nodes are respectively indicated by red or blue lines.

(B) Cytoscape visualization of pathway enrichment analysis performed on 1,330 super-enhancers identified across 5 ETMRs using ROSE; $q < 0.05$. MYCN/MAZ-regulated biological processes are indicated by red hubs and green lines.

(C) RNA-seq expression analyses of ETMRs with *C19MC* amplification (Amp) (n = 13) or gain (Gain) (n = 4), and other PBTs (n = 17). Significance was calculated using a t test. *$q < 0.05$. Data are presented as individual cases with means ± SEM, indicated.

(D) RNA-seq expression analyses of 0- to 37-week-old fetal brains derived from BrainSpan data. n = 3–45 samples depending on time point. Data are presented as means ± SEM.

(E) Dose-response curves and half maximal inhibitory concentration (IC_{50}) values for A664 vector control (blue) and A664-5miR (red) cell lines 72 h post-treatment with active isomer JQ1S; **doses with significantly different effects on A664 control and A664-5miR cell lines; **$p < 0.01$.

(F) qRT-PCR and western blot analyses of A664 vector control and A664-5miR cell lines treated with active JQ1S or inactive isomer JQ1R for 24 h.

(legend continued on next page)

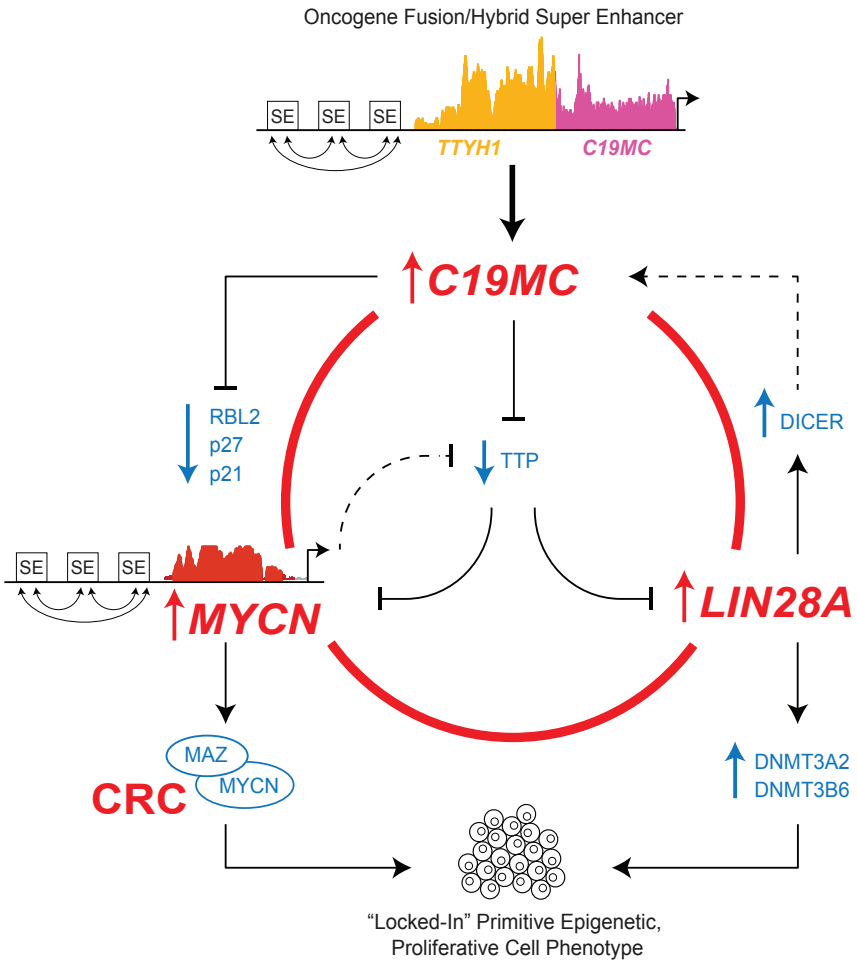

Figure 8. Hijacked Super-Enhancers Amplify a *C19MC*-LIN28A-MYCN Oncogenic Circuit to Drive ETMR Transformation

Schematic model of a *C19MC*-LIN28A-MYCN oncogenic circuit in ETMRs fueled by multiple feed-forward loops and powerfully amplified by *TTYH1-C19MC*- and *MYCN*-associated super-enhancers (SE), an MYCN-driven core transcriptional circuit (CRC), and LIN28A-mediated regulation of DICER1. *C19MC* silencing of critical cell-cycle proteins p21, p27, and RBL2 acts together with MYCN-driven proliferation and LIN28A-mediated epigenetic reprogramming to entrap an oncogenic, primitive epigenetic cell phenotype in ETMRs. Peaks represent H3K27Ac marks. Loops indicate DNA-DNA interactions. Solid and dashed lines, respectively, indicate functionally validated and predicted regulatory relationships.

regulation in ETMRs, as reported in other cancers (Molenaar et al., 2012; Powers et al., 2016), remains to be studied.

In addition to promoting cell proliferation, our RIP studies suggest that LIN28A plays a major role in ETMR epigenetic programming via direct binding and regulation of mRNAs encoding epigenetic regulators including DNMT3A and DNMT3B, which have isoform-restricted expression during brain development. While DNMT3A2, which functions in genomic imprinting and germ cell development (Ma et al., 2015; Nimura et al., 2006), is expressed in up to 16-week-old fetal brain, DNMT3B6 expression is highest in <8-week-old fetal brain. Interestingly, RNA-seq data suggest that DNMT3A2, as well as DNMT3B6, which is the only enzymatically active isoform expressed in ETMRs, are almost exclusively expressed in ETMRs and not other PBTs, underscoring the very distinct and primitive epigenetic features of this disease. Both DNMT3A2 and DNMT3B6 are detected in ETMRs with and without *C19MC* copy-number alterations (data not shown), indicating that these isoforms may reflect a common epigenetic cell state in these tumors that is promoted but not specifically activated by *C19MC*. Of note, we also identified DICER1, a key miRNA biogenesis gene, as a LIN28A upregulated target. Taken together with our previous observations of a *C19MC*-RBL2-DNMT3B axis (Kleinman et al., 2014), these observations indicate that *C19MC*, MYCN, and LIN28A act via parallel and synergistic circuits to drive and sustain a primitive, malignant epigenetic program in ETMRs.

In keeping with early embryonic epigenetic features of ETMRs, we observed that exogenous *C19MC* have limited transforming activity in postnatal murine neural precursors (our unpublished data). Consistent with our previous study that linked *C19MC* expression with Sonic hedgehog (SHH) and WNT developmental signaling in ETMRs (Li et al., 2009; Picard et al., 2012), we observed enrichment of multiple SHH and WNT pathway components, including GLI2 and AXIN2, in RIP studies indicating that *C19MC* may act via LIN28A to modulate these lineage-determining pathways. Interestingly embryonal tumors with histological and transcriptional features resembling human ETMRs have been reported by concurrent activation of SHH and WNT signaling in murine neural precursors (Neumann et al., 2017). However, these murine tumors lacked characteristic LIN28A expression patterns seen in human tumors, indicating that alternative strategies may be needed to model ETMRs.

Super-enhancers are clusters of enhancers that determine cell-type-specific transcriptional signatures by regulating master TFs or lineage-associated miRNAs, including miR290–295, which define cellular identity and origins (Suzuki et al., 2017; Whyte et al., 2013). Super-enhancers have also been

(G) miRNA qRT-PCR and western blot analyses of ETMR2373 cell lines treated with active JQ1S or inactive isomer JQ1R for 24 h.
In all cell line experiments, controls are indicated by Ctrl, data are presented as means ± SEM (n = 3); Significance was determined by unpaired two-tailed Student's t test; *p < 0.05; mRNA and miRNA expression are respectively normalized to actin, RNU6B, tubulin served as western blot loading controls.
See also Figure S7 and Table S7.

increasingly implicated in activation of driver oncogenes, and they have been shown to confer distinct tumor cell dependencies and sensitivities to drugs that target super-enhancer components (Loven et al., 2013). Our studies revealed that super-enhancers co-opted by *TTYH1-C19MC* gene fusions, and long-range *MYCN* promoter-enhancer interactions, were restricted to ETMRs and powerfully amplify a *C19MC*-LIN28A-MYCN oncogenic circuit. Notably, our enhancer mapping studies suggest that the functional status of *TTYH1*, *C19MC*, *LIN28A*, *MYCN*, and *DNMT3B6*, which comprise the core components of the *C19MC*-LIN28A-MYCN oncogenic circuit, most closely mirrors that of early neural stem cells from ~11-week-old fetal brain. Consistent with a super-enhancer-driven *C19MC*-MYCN dependency in ETMRs, we observed transient MYCN knockdown induced growth arrest in A664 cells (data not shown), while bromodomain inhibitor JQ1 induced death in A664 and A664-5miR cells. Notably, JQ1 treatment downregulated only key components of the oncogenic lineage circuit including MYCN, LIN28A, DNMT3B6, but not LIN28B, DNMT3A2, or DNMT1, which was mirrored by anti-miR-mediated targeting of endogenous *C19MC* in ETMR2373 cells. Thus, we propose that *C19MC* drives a distinct lineage-associated dependency and vulnerability in ETMRs.

Our collective findings in this study highlight ETMR as a developmental cancer arising in embryonic neural progenitors that is driven by hijacked lineage-specific signaling pathways. We identify cellular proliferation and embryonic epigenetic programming as key features of this disease, which is sustained by a unique potent super-enhancer-dependent oncogenic circuit vulnerable to bromodomain inhibition. Our data suggest that pharmacologic agents targeting BET/bromodomains may represent promising therapeutics for this recalcitrant orphan cancer.

STAR★METHODS

Detailed methods are provided in the online version of this paper and include the following:

- KEY RESOURCES TABLE
- CONTACT FOR REAGENT AND RESOURCE SHARING
- EXPERIMENTAL MODEL AND SUBJECT DETAILS
  - Human Tumors and Molecular Analyses
  - Cell Culture and Transfections
- METHOD DETAILS
  - Expression Constructs and Stable Cell Lines
  - Cell Growth, Cell Cycle Assay and JQ1 Treatment
  - RNA Extraction and qRT-PCR Analysis
  - Immuno-Histochemical (IHC) and Western Blotting Analysis
  - miRNA *In Situ* Hybridization Analysis
  - Luciferase Reporter Assays
  - Identification of *C19MC* Gene Targets
  - RNA Binding Protein Predictions
  - LIN28A RNA-Immunoprecipitation (RIP) and Sequencing
  - Methylation Analysis
  - Unsupervised Analysis of ETMR with Other Paediatric Brain Tumor
  - Genome Wide Copy Number Alteration Analysis with Methylation and SNP Arrays
  - Processing of miRNA Nanostring Data
  - RNAseq Analyses and Fusion Calling
  - Methylation and RNAseq Public Data
  - H3K27Ac ChIPseq Sample Preparation and Analysis
  - ATACseq Sample Preparation and Analysis
  - Mapping Long Range Enhancer Interaction Using C3D
  - Core Regulatory Circuitry (CRC) Analyses
  - Super-Enhancer Pathway Analysis
- DATA AND SOFTWARE AVAILABILITY
- QUANTIFICATION AND STATISTICAL ANALYSIS

ACCESSION NUMBERS

RNA-seq, H3K27Ac ChIP-seq, ATAC-seq, NanoString, methylation, and SNP array data are deposited at the European Genome-Phenome Archive, EGA Study Accession ID EGA:EGAS00001003437.

SUPPLEMENTAL INFORMATION

Supplemental Information can be found online at https://doi.org/10.1016/j.ccell.2019.06.002.

ACKNOWLEDGMENTS

S. Krumholtz and J. Loukides for assistance with graphics and technical contributions, The Rare Brain Tumor Consortium (http://www.rarebraintumorconsortium.ca) and tumor banks of contributing centers for tumor tissue. This project was funded by a Canadian Institutes of Health Research (CIHR) grant no. 137011 and b.r.a.i.n. child to A.H. T.S. is a CIHR Scholar.

AUTHOR CONTRIBUTIONS

A.H. conceived and supervised all of the experiments except for ChIP-seq analyses, which was supervised by J.N.R. RNA-seq, gene expression, NanoString, and copy-number analyses were performed by P.S.-C., I.M., T.S., B.H., N.P., and J.T. ATAC and ChIP assays were performed by P.S.-C., X.F., and S.C.M., and data analyses were performed by P.S.-C., I.M., and N.P., with advice from P.G. and S.C.M. CRC analyses was performed by I.M. and I.S. under supervision of C.Y.L. and A.H. Cellular, histopathologic, and biochemical assays were performed by P.S.-C., I.M., T.S., M.L., and D.P. Statistical analyses was performed by P.S.-C., I.M., and T.S. Tumor tissue and cell lines used in this study were provided by M.F., A.L., P.S.-P., E.R., L.M.H., N.G., T.E.V.M., S.L., H.N., T.-T.W., Y.-S.R., S.-K.K., L.M., R.G.G., J.F., D.J., J.C., L.L.-C., E.I.H., Y.W., A.R., G.Y.G., D.C., J.R.H., J.M., J.M.M.L., B.E., R.R., H.L., N.J., C.L.K., M.D.T., C.E.H., E.B., P.B.D., S.K.S., X.N.-L., and Y.D. D.B.-L. provided JQ1. P.S.-C., I.M., and A.H. wrote the manuscript with input from J.N.R. and S.C.M.

DECLARATION OF INTERESTS

P.S.-C. is employed at Regeneron Pharmaceuticals.

Received: February 11, 2019
Revised: April 26, 2019
Accepted: June 3, 2019
Published: July 8, 2019

REFERENCES

Agarwal, V., Bell, G.W., Nam, J.W., and Bartel, D.P. (2015). Predicting effective microRNA target sites in mammalian mRNAs. Elife 4. https://doi.org/10.7554/eLife.05005.

Aryee, M.J., Jaffe, A.E., Corrada-Bravo, H., Ladd-Acosta, C., Feinberg, A.P., Hansen, K.D., and Irizarry, R.A. (2014). Minfi: a flexible and comprehensive

Bioconductor package for the analysis of Infinium DNA methylation microarrays. Bioinformatics *30*, 1363–1369.

Bentwich, I., Avniel, A., Karov, Y., Aharonov, R., Gilad, S., Barad, O., Barzilai, A., Einat, P., Einav, U., Meiri, E., et al. (2005). Identification of hundreds of conserved and nonconserved human microRNAs. Nat. Genet. *37*, 766–770.

Bortolin-Cavaille, M.L., Dance, M., Weber, M., and Cavaille, J. (2009). C19MC microRNAs are processed from introns of large Pol-II, non-protein-coding transcripts. Nucleic Acids Res. *37*, 3464–3473.

Buenrostro, J.D., Wu, B., Chang, H.Y., and Greenleaf, W.J. (2015). ATAC-seq: a method for assaying chromatin accessibility genome-wide. Curr. Protoc. Mol. Biol. *109*, 21 29 21–29.

Cho, J., Chang, H., Kwon, S.C., Kim, B., Kim, Y., Choe, J., Ha, M., Kim, Y.K., and Kim, V.N. (2012). LIN28A is a suppressor of ER-associated translation in embryonic stem cells. Cell *151*, 765–777.

Cook, K.B., Kazan, H., Zuberi, K., Morris, Q., and Hughes, T.R. (2011). RBPDB: a database of RNA-binding specificities. Nucleic Acids Res. *39*, D301–D308.

Enright, A.J., John, B., Gaul, U., Tuschl, T., Sander, C., and Marks, D.S. (2003). MicroRNA targets in Drosophila. Genome Biol. *5*, R1.

Filippova, G.N., Fagerlie, S., Klenova, E.M., Myers, C., Dehner, Y., Goodwin, G., Neiman, P.E., Collins, S.J., and Lobanenkov, V.V. (1996). An exceptionally conserved transcriptional repressor, CTCF, employs different combinations of zinc fingers to bind diverged promoter sequences of avian and mammalian c-myc oncogenes. Mol. Cell. Biol. *16*, 2802–2813.

Gomez, S., Castellano, G., Mayol, G., Queiros, A., Martin-Subero, J.I., and Lavarino, C. (2015). DNA methylation fingerprint of neuroblastoma reveals new biological and clinical insights. Genom. Data *5*, 360–363.

Hovestadt, V., Remke, M., Kool, M., Pietsch, T., Northcott, P.A., Fischer, R., Cavalli, F.M., Ramaswamy, V., Zapatka, M., Reifenberger, G., et al. (2013). Robust molecular subgrouping and copy-number profiling of medulloblastoma from small amounts of archival tumour material using high-density DNA methylation arrays. Acta Neuropathol *125*, 913–916.

Huang, Q., Gumireddy, K., Schrier, M., le Sage, C., Nagel, R., Nair, S., Egan, D.A., Li, A., Huang, G., Klein-Szanto, A.J., et al. (2008). The microRNAs miR-373 and miR-520c promote tumour invasion and metastasis. Nat. Cell Biol. *10*, 202–210.

Johann, P.D., Erkek, S., Zapatka, M., Kerl, K., Buchhalter, I., Hovestadt, V., Jones, D.T.W., Sturm, D., Hermann, C., Segura Wang, M., et al. (2016). Atypical teratoid/rhabdoid tumors are comprised of three epigenetic subgroups with distinct enhancer landscapes. Cancer Cell *29*, 379–393.

Johnson, W.E., Li, C., and Rabinovic, A. (2007). Adjusting batch effects in microarray expression data using empirical Bayes methods. Biostatistics *8*, 118–127.

Jones, D.T., Jager, N., Kool, M., Zichner, T., Hutter, B., Sultan, M., Cho, Y.J., Pugh, T.J., Hovestadt, V., Stutz, A.M., et al. (2012). Dissecting the genomic complexity underlying medulloblastoma. Nature *488*, 100–105.

Kim, C.W., Vo, M.T., Kim, H.K., Lee, H.H., Yoon, N.A., Lee, B.J., Min, Y.J., Joo, W.D., Cha, H.J., Park, J.W., and Cho, W.J. (2012). Ectopic over-expression of tristetraprolin in human cancer cells promotes biogenesis of let-7 by down-regulation of Lin28. Nucleic Acids Res. *40*, 3856–3869.

Kim, D., Pertea, G., Trapnell, C., Pimentel, H., Kelley, R., and Salzberg, S.L. (2013). TopHat2: accurate alignment of transcriptomes in the presence of insertions, deletions and gene fusions. Genome Biol *14*, R36.

Kleinman, C.L., Gerges, N., Papillon-Cavanagh, S., Sin-Chan, P., Pramatarova, A., Quang, D.A., Adoue, V., Busche, S., Caron, M., Djambazian, H., et al. (2014). Fusion of TTYH1 with the C19MC microRNA cluster drives expression of a brain-specific DNMT3B isoform in the embryonal brain tumor ETMR. Nat. Genet. *46*, 39–44.

Kool, M., Jones, D.T., Jager, N., Northcott, P.A., Pugh, T.J., Hovestadt, V., Piro, R.M., Esparza, L.A., Markant, S.L., Remke, M., et al. (2014). Genome sequencing of SHH medulloblastoma predicts genotype-related response to smoothened inhibition. Cancer Cell *25*, 393–405.

Korshunov, A., Sturm, D., Ryzhova, M., Hovestadt, V., Gessi, M., Jones, D.T., Remke, M., Northcott, P., Perry, A., Picard, D., et al. (2014). Embryonal tumor with abundant neuropil and true rosettes (ETANTR), ependymoblastoma, and medulloepithelioma share molecular similarity and comprise a single clinicopathological entity. Acta Neuropathol. *128*, 279–289.

Lambert, S.R., Witt, H., Hovestadt, V., Zucknick, M., Kool, M., Pearson, D.M., Korshunov, A., Ryzhova, M., Ichimura, K., Jabado, N., et al. (2013). Differential expression and methylation of brain developmental genes define location-specific subsets of pilocytic astrocytoma. Acta Neuropathol. *126*, 291–301.

Lee, J.Y., Kim, H.J., Yoon, N.A., Lee, W.H., Min, Y.J., Ko, B.K., Lee, B.J., Lee, A., Cha, H.J., Cho, W.J., and Park, J.W. (2013). Tumor suppressor p53 plays a key role in induction of both tristetraprolin and let-7 in human cancer cells. Nucleic Acids Res. *41*, 5614–5625.

Li, M., Lee, K.F., Lu, Y., Clarke, I., Shih, D., Eberhart, C., Collins, V.P., Van Meter, T., Picard, D., Zhou, L., et al. (2009). Frequent amplification of a Chr19q13.41 microRNA polycistron in aggressive primitive neuroectodermal brain tumors. Cancer Cell *16*, 533–546.

Lichner, Z., Pall, E., Kerekes, A., Pallinger, E., Maraghechi, P., Bosze, Z., and Gocza, E. (2011). The miR-290-295 cluster promotes pluripotency maintenance by regulating cell cycle phase distribution in mouse embryonic stem cells. Differentiation *81*, 11–24.

Lin, C.Y., Erkek, S., Tong, Y., Yin, L., Federation, A.J., Zapatka, M., Haldipur, P., Kawauchi, D., Risch, T., Warnatz, H.J., et al. (2016). Active medulloblastoma enhancers reveal subgroup-specific cellular origins. Nature *530*, 57–62.

Louis, D.N., Perry, A., Reifenberger, G., von Deimling, A., Figarella-Branger, D., Cavenee, W.K., Ohgaki, H., Wiestler, O.D., Kleihues, P., and Ellison, D.W. (2016). The 2016 World Health organization classification of tumors of the central nervous system: a summary. Acta Neuropathol. *131*, 803–820.

Loven, J., Hoke, H.A., Lin, C.Y., Lau, A., Orlando, D.A., Vakoc, C.R., Bradner, J.E., Lee, T.I., and Young, R.A. (2013). Selective inhibition of tumor oncogenes by disruption of super-enhancers. Cell *153*, 320–334.

Ma, P., de Waal, E., Weaver, J.R., Bartolomei, M.S., and Schultz, R.M. (2015). A DNMT3A2-HDAC2 complex is essential for genomic imprinting and genome integrity in mouse oocytes. Cell Rep. *13*, 1552–1560.

Mack, S.C., Pajtler, K.W., Chavez, L., Okonechnikov, K., Bertrand, K.C., Wang, X., Erkek, S., Federation, A., Song, A., Lee, C., et al. (2018). Therapeutic targeting of ependymoma as informed by oncogenic enhancer profiling. Nature *553*, 101–105.

Mack, S.C., Witt, H., Piro, R.M., Gu, L., Zuyderduyn, S., Stutz, A.M., Wang, X., Gallo, M., Garzia, L., Zayne, K., et al. (2014). Epigenomic alterations define lethal CIMP-positive ependymomas of infancy. Nature *506*, 445–450.

Malik, A.N., Vierbuchen, T., Hemberg, M., Rubin, A.A., Ling, E., Couch, C.H., Stroud, H., Spiegel, I., Farh, K.K., Harmin, D.A., and Greenberg, M.E. (2014). Genome-wide identification and characterization of functional neuronal activity-dependent enhancers. Nat. Neurosci. *17*, 1330–1339.

Martin, M. (2011). Cutadapt removes adapter sequences from high-throughput sequencing reads. EMBnet J. *17*, 10–12.

Mehdi, T., Bailey, S.D., Guilhamon, P., and Lupien, M. (2018). C3D: a tool to predict 3D genomic interactions between cis-regulatory elements. Bioinformatics *35*, 877–879.

Merico, D., Isserlin, R., Stueker, O., Emili, A., and Bader, G.D. (2010). Enrichment map: a network-based method for gene-set enrichment visualization and interpretation. PLoS One *5*, e13984.

Mermel, C.H., Schumacher, S.E., Hill, B., Meyerson, M.L., Beroukhim, R., and Getz, G. (2011). GISTIC2.0 facilitates sensitive and confident localization of the targets of focal somatic copy-number alteration in human cancers. Genome Biol. *12*, R41.

Molenaar, J.J., Domingo-Fernandez, R., Ebus, M.E., Lindner, S., Koster, J., Drabek, K., Mestdagh, P., van Sluis, P., Valentijn, L.J., van Nes, J., et al. (2012). LIN28B induces neuroblastoma and enhances MYCN levels via let-7 suppression. Nat. Genet. *44*, 1199–1206.

Mootha, V.K., Lindgren, C.M., Eriksson, K.F., Subramanian, A., Sihag, S., Lehar, J., Puigserver, P., Carlsson, E., Ridderstrale, M., Laurila, E., et al. (2003). PGC-1alpha-responsive genes involved in oxidative phosphorylation are coordinately downregulated in human diabetes. Nat. Genet. *34*, 267–273.

Murphy, B.L., Obad, S., Bihannic, L., Ayrault, O., Zindy, F., Kauppinen, S., and Roussel, M.F. (2013). Silencing of the miR-17~92 cluster family inhibits medulloblastoma progression. Cancer Res. *73*, 7068–7078.

Neumann, J.E., Wefers, A.K., Lambo, S., Bianchi, E., Bockstaller, M., Dorostkar, M.M., Meister, V., Schindler, P., Korshunov, A., von Hoff, K., et al. (2017). A mouse model for embryonal tumors with multilayered rosettes uncovers the therapeutic potential of Sonic-hedgehog inhibitors. Nat. Med. *23*, 1191–1202.

Nilsen, G., Liestol, K., Van Loo, P., Moen Vollan, H.K., Eide, M.B., Rueda, O.M., Chin, S.F., Russell, R., Baumbusch, L.O., et al. (2012). Copynumber: efficient algorithms for single- and multi-track copy number segmentation. BMC Genomics *13*, 591.

Nimura, K., Ishida, C., Koriyama, H., Hata, K., Yamanaka, S., Li, E., Ura, K., and Kaneda, Y. (2006). Dnmt3a2 targets endogenous Dnmt3L to ES cell chromatin and induces regional DNA methylation. Genes Cells *11*, 1225–1237.

Northcott, P.A., Lee, C., Zichner, T., Stutz, A.M., Erkek, S., Kawauchi, D., Shih, D.J., Hovestadt, V., Zapatka, M., Sturm, D., et al. (2014). Enhancer hijacking activates GFI1 family oncogenes in medulloblastoma. Nature *511*, 428–434.

Paraskevopoulou, M.D., Georgakilas, G., Kostoulas, N., Vlachos, I.S., Vergoulis, T., Reczko, M., Filippidis, C., Dalamagas, T., and Hatzigeorgiou, A.G. (2013). DIANA-microT web server v5.0: service integration into miRNA functional analysis workflows. Nucleic Acids Res *41*, W169–W173.

Peng, S., Chen, L.L., Lei, X.X., Yang, L., Lin, H., Carmichael, G.G., and Huang, Y. (2011). Genome-wide studies reveal that Lin28 enhances the translation of genes important for growth and survival of human embryonic stem cells. Stem Cells *29*, 496–504.

Pfister, S., Remke, M., Castoldi, M., Bai, A.H., Muckenthaler, M.U., Kulozik, A., von Deimling, A., Pscherer, A., Lichter, P., and Korshunov, A. (2009). Novel genomic amplification targeting the microRNA cluster at 19q13.42 in a pediatric embryonal tumor with abundant neuropil and true rosettes. Acta Neuropathol. *117*, 457–464.

Picard, D., Miller, S., Hawkins, C.E., Bouffet, E., Rogers, H.A., Chan, T.S., Kim, S.K., Ra, Y.S., Fangusaro, J., Korshunov, A., et al. (2012). Markers of survival and metastatic potential in childhood CNS primitive neuro-ectodermal brain tumours: an integrative genomic analysis. Lancet Oncol. *13*, 838–848.

Powers, J.T., Tsanov, K.M., Pearson, D.S., Roels, F., Spina, C.S., Ebright, R., Seligson, M., de Soysa, Y., Cahan, P., Theissen, J., et al. (2016). Multiple mechanisms disrupt the let-7 microRNA family in neuroblastoma. Nature *535*, 246–251.

Rajaram, V., Knezevich, S., Bove, K.E., Perry, A., and Pfeifer, J.D. (2007). DNA sequence of the translocation breakpoints in undifferentiated embryonal sarcoma arising in mesenchymal hamartoma of the liver harboring the t(11;19)(q11;q13.4) translocation. Genes Chromosomes Cancer *46*, 508–513.

Reimand, J., Arak, T., Adler, P., Kolberg, L., Reisberg, S., Peterson, H., and Vilo, J. (2016). g:Profiler—a web server for functional interpretation of gene lists (2016 update). Nucleic Acids Res. *44*, W83–W89.

Rippe, V., Dittberner, L., Lorenz, V.N., Drieschner, N., Nimzyk, R., Sendt, W., Junker, K., Belge, G., and Bullerdiek, J. (2010). The two stem cell microRNA gene clusters C19MC and miR-371-3 are activated by specific chromosomal rearrangements in a subgroup of thyroid adenomas. PLoS One *5*, e9485.

Robinson, J.T., Thorvaldsdottir, H., Winckler, W., Guttman, M., Lander, E.S., Getz, G., and Mesirov, J.P. (2011). Integrative genomics viewer. Nat. Biotechnol. *29*, 24–26.

Saint-Andre, V., Federation, A.J., Lin, C.Y., Abraham, B.J., Reddy, J., Lee, T.I., Bradner, J.E., and Young, R.A. (2016). Models of human core transcriptional regulatory circuitries. Genome Res. *26*, 385–396.

Schuijers, J., Manteiga, J.C., Weintraub, A.S., Day, D.S., Zamudio, A.V., Hnisz, D., Lee, T.I., and Young, R.A. (2018). Transcriptional dysregulation of MYC reveals common enhancer-docking mechanism. Cell Rep. *23*, 349–360.

Shannon, P., Markiel, A., Ozier, O., Baliga, N.S., Wang, J.T., Ramage, D., Amin, N., Schwikowski, B., and Ideker, T. (2003). Cytoscape: a software environment for integrated models of biomolecular interaction networks. Genome Res. *13*, 2498–2504.

Spence, T., Perotti, C., Sin-Chan, P., Picard, D., Wu, W., Singh, A., Anderson, C., Blough, M.D., Cairncross, J.G., Lafay-Cousin, L., et al. (2014a). A novel C19MC amplified cell line links Lin28/let-7 to mTOR signaling in embryonal tumor with multilayered rosettes. Neuro Oncol. *16*, 62–71.

Spence, T., Sin-Chan, P., Picard, D., Barszczyk, M., Hoss, K., Lu, M., Kim, S.K., Ra, Y.S., Nakamura, H., Fangusaro, J., et al. (2014b). CNS-PNETs with C19MC amplification and/or LIN28 expression comprise a distinct histogenetic diagnostic and therapeutic entity. Acta Neuropathol. *128*, 291–303.

Sturm, D., Orr, B.A., Toprak, U.H., Hovestadt, V., Jones, D.T., Capper, D., Sill, M., Buchhalter, I., Northcott, P.A., Leis, I., et al. (2016). New brain tumor entities emerge from molecular classification of CNS-PNETs. Cell *164*, 1060–1072.

Sturm, D., Witt, H., Hovestadt, V., Khuong-Quang, D.A., Jones, D.T., Konermann, C., Pfaff, E., Tonjes, M., Sill, M., Bender, S., et al. (2012). Hotspot mutations in H3F3A and IDH1 define distinct epigenetic and biological subgroups of glioblastoma. Cancer Cell *22*, 425–437.

Suzuki, H.I., Young, R.A., and Sharp, P.A. (2017). Super-enhancer-mediated RNA processing revealed by integrative MicroRNA network analysis. Cell *168*, 1000–1014.e15.

Torchia, J., Golbourn, B., Feng, S., Ho, K.C., Sin-Chan, P., Vasiljevic, A., Norman, J.D., Guilhamon, P., Garzia, L., Agamez, N.R., et al. (2016). Integrated (epi)-Genomic analyses identify subgroup-specific therapeutic targets in CNS rhabdoid tumors. Cancer Cell *30*, 891–908.

Trapnell, C., Roberts, A., Goff, L., Pertea, G., Kim, D., Kelley, D.R., Pimentel, H., Salzberg, S.L., Rinn, J.L., and Pachter, L. (2012). Differential gene and transcript expression analysis of RNA-seq experiments with TopHat and Cufflinks. Nat. Protoc. *7*, 562–578.

Triche, T.J., Jr., Weisenberger, D.J., Van Den Berg, D., Laird, P.W., and Siegmund, K.D. (2013). Low-level processing of Illumina Infinium DNA methylation BeadArrays. Nucleic Acids Res. *41*, e90.

Viswanathan, S.R., Powers, J.T., Einhorn, W., Hoshida, Y., Ng, T.L., Toffanin, S., O'Sullivan, M., Lu, J., Phillips, L.A., Lockhart, V.L., et al. (2009). Lin28 promotes transformation and is associated with advanced human malignancies. Nat. Genet. *41*, 843–848.

Wang, B., Mezlini, A.M., Demir, F., Fiume, M., Tu, Z., Brudno, M., Haibe-Kains, B., and Goldenberg, A. (2014). Similarity network fusion for aggregating data types on a genomic scale. Nat. Methods *11*, 333–337.

Wei, T., and Simko, V.J.R.p. v. (2013). corrplot: Visualization of a correlation matrix *230*, 11.

Whyte, W.A., Orlando, D.A., Hnisz, D., Abraham, B.J., Lin, C.Y., Kagey, M.H., Rahl, P.B., Lee, T.I., and Young, R.A. (2013). Master transcription factors and mediator establish super-enhancers at key cell identity genes. Cell *153*, 307–319.

Wilbert, M.L., Huelga, S.C., Kapeli, K., Stark, T.J., Liang, T.Y., Chen, S.X., Yan, B.Y., Nathanson, J.L., Hutt, K.R., Lovci, M.T., et al. (2012). LIN28 binds messenger RNAs at GGAGA motifs and regulates splicing factor abundance. Mol. Cell *48*, 195–206.

Yu, J., Vodyanik, M.A., Smuga-Otto, K., Antosiewicz-Bourget, J., Frane, J.L., Tian, S., Nie, J., Jonsdottir, G.A., Ruotti, V., Stewart, R., et al. (2007). Induced pluripotent stem cell lines derived from human somatic cells. Science *318*, 1917–1920.

Zeid, R., Lawlor, M.A., Poon, E., Reyes, J.M., Fulciniti, M., Lopez, M.A., Scott, T.G., Nabet, B., Erb, M.A., Winter, G.E., et al. (2018). Enhancer invasion shapes MYCN-dependent transcriptional amplification in neuroblastoma. Nat. Genet. *50*, 515–523.

Zhang, Y., Liu, T., Meyer, C.A., Eeckhoute, J., Johnson, D.S., Bernstein, B.E., Nusbaum, C., Myers, R.M., Brown, M., Li, W., and Liu, X.S. (2008). Model-based analysis of ChIP-seq (MACS). Genome Biol. *9*, R137.

Zhou, L., Picard, D., Ra, Y.S., Li, M., Northcott, P.A., Hu, Y., Stearns, D., Hawkins, C., Taylor, M.D., Rutka, J., et al. (2010). Silencing of thrombospondin-1 is critical for myc-induced metastatic phenotypes in medulloblastoma. Cancer Res *70*, 8199–8210.

STAR★METHODS

KEY RESOURCES TABLE

REAGENT or RESOURCE	SOURCE	IDENTIFIER
Antibodies		
Anti-p21 (12D1)	Cell Signaling	Cat# 2947; RRID: AB_823586
Anti-p27 (57)	BD Biosciences	Cat# 610242; RRID: AB_397637
Anti-RBL2	Sigma-Aldrich	Cat# HPA019703; RRID: AB_1856106
Anti-LIN28A (A177)	Cell Signaling	Cat# 3978; RRID: AB_2297060
Anti-LIN28B	Cell Signaling	Cat# 4196; RRID: AB_2135047
Anti-N-MYC (NCM II 100)	Millipore	Cat# MABE333; RRID: AB_2266879
Anti-MYC (9E10)	In-house (Zhou et al., 2010)	N/A
Anti-SALL4 (D16H12)	Cell Signaling	Cat# 8459; RRID: AB_10949321
Anti-SOX2 (D6D9)	Cell Signaling	Cat# 3579; RRID: AB_2195767
Anti-TTP	Abcam	Cat# ab83579; RRID: AB_10861702
Anti-DNMT1 (D63A6)	Cell Signaling	Cat# 5032; RRID: AB_10548197
Anti-DNMT3A (D23G1)	Cell Signaling	Cat# 3598; RRID: AB_2277449
Anti-DNMT3B (H230)	Santa Cruz Biotechnology	Cat# sc20704; RRID: AB_2094125
Anti-DICER	Cell Signaling	Cat# 3363; RRID: AB_2093073
Anti-MAZ (133.7)	Santa Cruz Biotechnology	Cat# sc130915; RRID: AB_2235125
Anti-BRD2 (D89B4)	Cell Signaling	Cat# 5848; RRID: AB_10835146
Anti-PARP	Cell Signaling	Cat# 9542; RRID: AB_2160739
Anti-α-tubulin	Sigma-Aldrich	Cat# T9026; RRID: AB_477593
Anti-LIN28A	Abcam	Cat# ab46020; RRID: AB_776033
Anti-rabbit IgG	Santa Cruz Biotechnology	Cat# sc2027; RRID: AB_737197
Anti-H3K27Ac	Active Motif	Cat# 39133; RRID: AB_2561016
Biological Samples		
Human primary ETMR tumor samples	This paper	N/A
Critical Commercial Assays		
Dual-Luciferase Reporter Assay System	Promega	Cat# E1910
RNA-Chip IT	Active Motif	Cat# 53024
Deposited Data		
LIN28A RIPseq on A664 cells	This paper	EGA: EGAD00001004802
RNAseq on ETMR samples	This paper	EGA: EGAD00001004803
ATACseq on ETMR samples	This paper	EGA: EGAD00001004805
H3K27Ac ChIPseq on ETMR samples	This paper	EGA: EGAD00001004809
Copy number on ETMR samples	This paper	EGA: EGAD00010001667
Methylation on ETMR samples	This paper	EGA: EGAD00010001669
Methylation on medulloblastoma samples	(Kool et al., 2014)	GEO: GSE49377
Methylation on medulloblastoma samples	(Hovestadt et al., 2013)	GEO: GSE75153
Methylation on neuroblastoma samples	(Gomez et al., 2015)	GEO: GSE54719
Methylation on AT/RT samples	(Johann et al., 2016)	GEO: GSE70460
Methylation on AT/RT samples	(Torchia et al., 2016)	EGA: EGAS00001000506
Methylation on PNET samples	(Sturm et al., 2016)	GEO: GSE73801
RNAseq on ETMR samples	(Kleinman et al., 2014)	SRA: SRP032476
Experimental Models: Cell Lines		
Daoy	ATCC	RRID: CVCL_1167
UW228	ATCC	RRID: CVCL_8585

(*Continued on next page*)

Continued

REAGENT or RESOURCE	SOURCE	IDENTIFIER
PFSK	ATCC	RRID: CVCL_1642
HEK293	ATCC	RRID: CVCL_0045
NCCIT	ATCC	RRID: CVCL_1451
hf5205	(Li et al., 2009)	N/A
A664	(Spence et al., 2014b)	N/A
ETMR2373	This paper	N/A
Oligonucleotides		
Primer sequences; see Table S8	This paper	N/A
Recombinant DNA		
Plasmid: pcDH-EF1-copGFP	System Biosciences	Cat# CD511B-1
Plasmid: pcDH-EF1-copRFP	System Biosciences	Cat# CD521B-1
pcDH-CMV-EF1-5miR-GFP	This paper	N/A
pcDH-CMV-EF1-LIN28A-RFP	This paper	N/A
Plasmid: pGEM-LIN28A	Addgene (Yu et al., 2007)	Addgene Cat# 16350
pcDNA3.1/nFlag-TTP	This paper	N/A
Plasmid: pmirGLO Dual-Luciferase miRNA target expression vector	Promega	Cat# E1330
Software and Algorithms		
TargetScan	Agarwal et al., 2015	http://www.targetscan.org/vert_72/
miRanda	Enright et al., 2003	http://www.microrna.org/microrna/home.do
DIANA	Paraskevopoulou et al., 2013	http://diana.imis.athena-innovation.gr/DianaTools/index.php?r=microT_CDS/index
RNA Binding Protein Data Base	Cook et al., 2011	http://rbpdb.ccbr.utoronto.ca/
Gene Set Enrichment Analysis	Mootha et al., 2003	http://software.broadinstitute.org/cancer/software/gsea/wiki/index.php/Gsea_papers
FlowJo	Tree Star, Inc.	https://www.flowjo.com/
GraphPad Prism 7.0	GraphPad Software, Inc.	https://www.graphpad.com/
minfi (v1.20.2)	Aryee et al., 2014	http://bioconductor.org/packages/release/bioc/html/minfi.html
GISTIC2 (v03172017)	Mermel et al., 2011	ftp://ftp.broadinstitute.org/pub/GISTIC2.0/GISTICDocumentation_standalone.htm
CopyNumber package	Nilsen et al., 2012	https://bioconductor.org/packages/release/bioc/html/copynumber.html
ComBat	Johnson et al., 2007	http://software.broadinstitute.org/cancer/software/genepattern/modules/docs/ComBat/3
Cutadapt (v1.10)	Martin et al., 2011	https://cutadapt.readthedocs.io/en/stable/
TopHat (v2.1.0)	Kim et al., 2013	https://ccb.jhu.edu/software/tophat/index.shtml
Integrative Genomics Viewer (v2.3.72)	Robinson et al., 2011	http://software.broadinstitute.org/software/igv/home
Cufflinks RNAseq assembly suit (v2.2.1)	Trapnell et al., 2012	http://cole-trapnell-lab.github.io/cufflinks/
Cross Cell-type Correlation based on DNA accessibility (C3D)	Mehdi et al., 2018	https://github.com/LupienLabOrganization/C3D
corrplot	Wei and Simko, 2013	http://CRAN.R-project.org/package=corrplot
MACS2	Zhang et al., 2008	https://github.com/taoliu/MACS/wiki/Advanced%3A-Call-peaks-using-MACS2-subcommands
ROSE	Whyte et al., 2013	http://younglab.wi.mit.edu/super_enhancer_code.html
CRC Mapper	Saint-Andre et al., 2016	https://bitbucket.org/young_computation/crcmapper
Enrichment Map application	Merico et al., 2010	http://baderlab.org/Software/EnrichmentMap
Cytoscape	Shannon et al., 2003	https://cytoscape.org/

CONTACT FOR REAGENT AND RESOURCE SHARING

Further information and requests for resources and reagents should be directed to and will be fulfilled by the Lead Contact, Annie Huang (annie.huang@sickkids.ca).

EXPERIMENTAL MODEL AND SUBJECT DETAILS

Human Tumors and Molecular Analyses

Tumor samples (90 primary ETMRs and 42 other PBTs) were collected through the Rare Brain Tumor Consortium and Registry (http://www.rarebraintumorconsortium.ca/) with informed consent as per protocols approved by the Hospital for Sick Children. Details of molecular analyses performed on tumor samples are listed in Table S1.

Cell Culture and Transfections

Daoy (source: male), UW228 (source: female), PFSK (source: male), NCCIT (source: male) and HEK293 (source: female) cells were purchased from ATCC and cultured in DMEM or RPMI-1640 medium supplemented with 10% fetal bovine serum (FBS). A664 cells (source: female) were derived from a primary cerebral medulloepithelioma (Spence et al., 2014b) and hNSC line hf5205 (source: female) was generously provided by Dr. Peter Dirks. ETMR2373 (source: male) cells were generously provided by Drs. Yuchen Du and Xiao-Nan Li. A664, hNSC hf5205 and ETMR2373 cells were cultured in NeuroCult media supplemented with 2 mM L-glutamine, 2 μg/mL Heparin, 75 μg/mL BSA, 10 ng/mL hEGF, 10 ng/mL bFGF, 1x B27 and 1x N2 supplements. All cell lines were incubated at 4% O_2 in a humidity-controlled environment (37°C, 5% CO_2). All cells were utilized before passage 10 and treated in exponential growth phase at ~70% confluency. hNSC 3-10 were obtained from various sources as described in Table S1. Transient transfection were performed with plasmid DNA or scramble/LIN28A-specific siRNA (Dharmacon, Cat#D-001810-01/J-018411-09) using Fugene (Promega, Cat#E2691) or Lipofectamine 2000 (Life Technologies, Cat#11668019) as per the manufacturer's protocols.

METHOD DETAILS

Expression Constructs and Stable Cell Lines

5miR expression plasmid was generated by designing a cluster of 5 *(miR520g*, *miR519a*, *miR517c*, *miR517a and miR512-3p) miRNA* precursor stem loop structures in a pcDH-CMV-MCS-EF1-copGFP vector and synthesized by System Biosciences. LIN28A expression construct (Yu et al., 2007) was obtained from Addgene (Cat#16350). Both constructs were sub-cloned into pcDH-CMV-EF1-copGFP/RFP (System Biosciences, Cat#CD511B-1/CD512B-1). TTP expression construct was obtained from SIDNET (The Hospital for Sick Children) and cloned into a pcDNA3.1/nFLAG expression construct. Lentivirus was generated and used for stable cell lines generation as per the Hospital for Sick Children safety guidelines. Expression of *C19MC* miRNAs and LIN28A were confirmed with qRT-PCR and/or western blotting.

Cell Growth, Cell Cycle Assay and JQ1 Treatment

Between 500-2000 cells/well were seeded in triplicate in 96-well plates in 100 μl of culture media and incubated overnight. Cell growth was evaluated daily for a period of 5-7 days upon addition of 20 μl/well of MTS reagent (Promega, Cat#G3582) and viable cell numbers were determined at absorbance 575 nm using Versamax microplate reader (Molecular Devices). For cell cycle analysis, 1E6 cells were fixed with ice-cold 70% ethanol, washed and treated with 100 μg/mL RNaseA, 50 μg/mL propidium iodide and 0.1% NP-40. Cells were filtered through 85-μm Nitex mesh and followed by fluorescence activated cell sorting (FACS) analysis. The proportion of cell in different cell cycle phases was determined using FlowJo software (Tree Star).

To determine IC50 for JQ1 treatments, A664, A664-pcDH and A664-5miR cells were seeded at 4,000 cells/well in a 96 well plate, allowed to adhere overnight and treated with JQ1 (generously provided by Dr. Dalia Barsyte-Lovejoy, Structural Genomics Consortium, University of Toronto) the following day. Cell viability was assessed using Alamar Blue at 72 hr post-treatment using an 8-point dose curve with drug doses from 0.1 nM-10 μM. Viable cell percentage for each concentration was determined relative to DMSO control. IC50 values were calculated using GraphPad Prism 7.0. A664 cells were treated with 570 nM JQ1R and JQ1S for cell growth assays or harvested 24 hr post-treatment for biochemical analysis. All cellular assays were performed in triplicate.

RNA Extraction and qRT-PCR Analysis

RNA was harvested via Trizol extraction as per manufacturer's instructions. cDNAs were synthesized from high quality RNA using High Capacity cDNA Reverse Transcriptase Kit (Applied Biosystem, Cat#4368814) and qRT-PCR analyses were performed using SYBR Select (Thermo Scientific, Cat#4472908) with custom designed PCR primers to amplify invariant exons or exon-exon junctions (For primer sequences, see Table S8). mRNA expression was calculated using the $2^{-\Delta\Delta CT}$ method; genes with Ct values $\geq$30 were excluded from analysis. Data was normalized to actin expression.

microRNA qRT-PCR was performed using 10 ng of RNA reversed transcribed using microRNA-specific stem-loop reverse transcription primers and TaqMan microRNA Reverse Transcription Kit (Thermo Fisher Scientific, Cat#4366596). miRNA qRT-PCR was performed using TaqMan Universal PCR Master Mix no AmpErase UNG (Thermo Fisher Scientific, Cat#4324018) and individual microRNA PCR probes. Data was normalized to RNU6B expression. All qRT-PCR analyses were performed n=3.

Immuno-Histochemical (IHC) and Western Blotting Analysis

For IHC studies, a heat-induced antigen retrieval process was used, followed by blocking of endogenous peroxidase and biotin. Primary antibodies against p21 (Cell signaling, Cat#2947), p27 (BD Biosciences, Cat#610242) and RBL2 (Sigma Aldrich, Cat#HPA019703) were used. Antibody reactivity was visualized using VectaStain ABC detection kit (Vector Laboratories, Cat#PK-4000). For western blot analyses, whole cell lysates were prepared using cytosol lysis buffer and probed with various antibodies using standard protocols. (For antibodies, see Key Resources Table). Immunoreactivity was detected using secondary anti-species horseradish peroxidase–conjugated antibodies (GE Healthcare, #NAV934/931) and Chemi-luminescence Reagent Plus (PerkinElmer, Cat#NEL103001EA).

miRNA *In Situ* Hybridization Analysis

miRNA *in situ* hybridization (ISH) was performed using Alexa 488 (Thermo Fisher, Cat# A20181) coupled miR520g or scrambled probes (Qiagen) on sequentially sectioned formalin fixed paraffin embedded primary ETMR using miRCURY LNA miRNA ISH Optimization Kit (Qiagen, Cat#339451). Signals were amplified using Tyramide Signal Amplification kit (Thermo Scientific, Cat#B40953). Fluorescence was detected using the Pannoramic 250 Flash series digital scanner. To compare miRNA amplified tumor cells with protein levels of p21, p27 and RBL2, we performed IHC analysis on sequentially sectioned tumors of the same ETMR and located the same geographical region on the tumor for all analyses.

Luciferase Reporter Assays

To assess direct effects of 5miR on target genes, 3'UTR constructs of p21, p27 and TTP from corresponding full lengths genes (SPARC, Hospital for Sick Children; Canada) were sub-cloned into a pmirGLO Dual-Luciferase miRNA target expression vector (Promega, Cat#E1330). *C19MC* binding sites were identified using miRNA target prediction algorithms (Targetscan, miRanda and DIANA – see Table S2) and seed sequences mutated using QuiKChange Site directed mutagenesis kit (Stratagene, Cat#200524). For luciferase assays, stable UW228-pcDH/miR520g/5miR cells were seeded at 0.3E5/well in triplicate in a 12-well plate and transfected with empty pmiRGLO, wild-type, mutated target gene 3'UTR or a control miR520g complementary (520-t) vector. Cells were harvested 48 hours post-transfection using Dual-Luciferase Reporter Assay System (Promega, Cat#E1910) and luciferase activity measured using the Lumat LB 9507 tube luminometer. Luciferase activity was normalized to empty pmiRGLO vector and Renilla. All assays were performed n=3.

Identification of *C19MC* Gene Targets

To identify which of the 179 downregulated cell cycle genes may be targeted by the 5 major classes of *C19MC* miRNA families (miR-520, 519, 517a/c and 512), we utilized three distinct miRNA target predictions algorithms including TargetScan, miRanda and DIANA. Our strict criteria included a) whether the 3'UTR of these genes contained $\geq$2 *C19MC* binding sites, b) whether the same binding site locations were conserved across all three algorithms and c) whether the sites were evolutionarily conserved. Based on these criteria, 11/179 genes emerged as *C19MC* candidate targets. H3K27Ac and ATACseq data were used to validate the functional status of the 11 candidate targets in primary ETMR, which revealed only 5 genes (p21, p27, *RBL2*, *CCND2* and *AHR*) that exhibited active enhancers and open chromatin, indicating these genes were transcriptionally active in ETMRs.

RNA Binding Protein Predictions

The RNA Binding Protein Data Base software (http://rbpdb.ccbr.utoronto.ca/) (Cook et al., 2011) was used to predict RNA binding protein targeted to the 3'UTR of *LIN28A*, *MYCN*, *LIN28B* and *MYC*.

LIN28A RNA-Immunoprecipitation (RIP) and Sequencing

LIN28A RIP was performed using RNA-Chip IT (Active Motif, Cat#53024) using previously described methods (Cho et al., 2012; Wilbert et al., 2012). Briefly, formaldehyde cross-linked chromatin from 1E6 A664 cells was fragmented via water bath sonication to 100-1000 bp fragments. Samples were treated with DNase I and RIP performed using 4 μg LIN28A antibody (Abcam, Cat#ab46020) or normal rabbit IgG (Santa Cruz Biotechnology, Cat#sc2027) and rotated overnight at 4°C. Chromatin was de-crosslinked using Proteinase K and RNA isolated via Trizol extraction followed by DNase I treatment. DNA libraries were prepared using Clontech Ultralow kit and sequenced by paired-end Illumina HiSeq 2500 sequencing at the Donnelly Sequencing Centre (University of Toronto). Alignment and peaks were called using MACS2 software (v2.1.0.20140616) (Zhang et al., 2008). Gene Set Enrichment Analysis (Mootha et al., 2003) was performed to identify transcriptional networks and visualized using Cytoscape (Shannon et al., 2003).

Methylation Analysis

DNA from frozen tissue and formalin-fixed, paraffin-embedded (FFPE) materials were analyzed with the Illumina Infinium Human Methylation 450k and MethylationEPIC arrays according to manufacturer's instructions and published methods (Torchia et al., 2016; Triche et al., 2013). To integrate both array platforms, only probes that are found in the 450k array were retained. Background correction and dye-bias normalization were performed using the normal-exponential out-of-band method from the R package *minfi* (v1.20.2) (Aryee et al., 2014). CpG sites with detection p value <0.01 were retained for analysis and only samples with <5% failed probes were retained. The most variable methylated probes ranging from 5,000-15,000 (s.d.>0.3) were selected for all downstream analysis. All analyses were performed in the R environment (3.3.3) except when noted.

Unsupervised Analysis of ETMR with Other Paediatric Brain Tumor

For unsupervised analyses of ETMR and other PBTs, raw idats or normalized beta matrix values of methylation data for medulloblastoma (Jones et al., 2012), atypical teratoid/rhabdoid tumor (ATRT) (Johann et al., 2016; Torchia et al., 2016), neuroblastoma (Gomez et al., 2015), pilocytic astrocytoma (Lambert et al., 2013), ependymoma (Mack et al., 2014; Sturm et al., 2016), high grade glioma (Sturm et al., 2012, 2016), pineoblastoma (Sturm et al., 2016) were downloaded from GEO and combined with in-house samples in the pipeline described above. Principal component analysis (PCA) was performed using R package *stats* (v3.3.3) and the top 50 principle component used for tSNE analysis with the *Rtsne* package (v0.13). 5-50 perplexity were tested to find the optimal settings. Other non-default settings: pca=F, max_iter=5000, theta=0. Each of the aforementioned tumor group form distinct entities with no batch effect by material type and processing date was observed with distinct clustering of samples according to tumor subtype.

Genome Wide Copy Number Alteration Analysis with Methylation and SNP Arrays

Genome-wide copy number analyses were performed using SNP (n=33) and methylation array data (n=77). For SNP array analyses, the Illumina OmniQuad array platform was used. Probe fluorescence intensity normalization and transformation was performed using Illumina Genome Studio (v. 2011.1 Genotyping Module 1.9.4) and represented as LogR ratio ($Log2[R_{experiment}/R_{controlset}]$) and B-allele frequency (BAF) using hg19 human reference genome. ASCAT (Allele Specific Copy Number Analysis of Tumors) was performed to assess tumor purity and ploidy using its control-free analysis function at default parameters. Methylation array data was analysed using the R package *conumee* for the 450k array and EPIC array (v 1.2.0 and 1.8.0 respectively) using default settings. For both methylation and SNP array data, tumor probe level LogR and segmented profiles were visualize using the R package *Gviz* (version 1.18.2). Recurrent focal and arm-level structural alteration was analyzed using GISTIC2 (v03172017). At least half of the chromosome arm must be affected to be considered as a broad event for arm-level structural alteration analysis. For focal alterations, -0.3 and 0.3 deletion and gain threshold respectively to identify driver events with the HLA region Chr6:28477797-33448354 excluded. For both type of analysis, significant alterations were evaluated based on Benjamin-Hochberg false discovery rate corrected *p* values for each marker from comparing the score at each locus to background score generated by random permutation of marker location with $q \leq 0.01$.

Normalized and log2-transformed copy number measurements were imported and analysed using *CopyNumber* package pipeline (Nilsen et al., 2012) to identify segments with similar copy number. Binned segmentation results of conumee output from methylation arrays from all primary ETMR (N=77) were used to generate a composite copy number plot. Average Log2 levels were calculated across overlapping segments with noise removal from HLA region and end of chromosome arm using an in-house script. The results were plotted using Circos (v0.69).

Processing of miRNA Nanostring Data

Total RNA (100ng) from 21 ETMRs with *C19MC* structural alterations and 28 other PBTs was prepared with nCounter miRNA Sample Prep Kit according to standard protocol. miRNA expression profiling was conducted with human v1, v2, or v3 miRNA panel on nCounter miRNA expression platform (NanoString Technologies, Seattle, WA) according to manufacturer's protocol. Signal normalization was done using nSolver Analysis and batch corrected using ComBat (Johnson et al., 2007). 565 miRNAs overlapped between all three versions and was used for further analyses. Fold change and supervised t-test with FDR correction was calculated between the ETMRs and other PBTs.

RNAseq Analyses and Fusion Calling

RNAseq of tumor and cell lines were performed at the Princess Margaret Genomics Centre (Toronto, Ontario). RNA was prepared using either the IlluminaTruSeq RNA sample preparation kit for poly-adenylated mRNA or Illumina RiboZero Stranded library preparation kit for total RNA with an average of 97.64 million and 92.13 million paired-end reads per sample respectively. Adapter sequences were trimmed using Cutadapt (v 1.10) and aligned to human reference genome hg19 using TopHat (v2.1.0). Gene expression values were represented as FPKM values generated from RNAseq alignments using cuffquant and cuffnorm programs within the Cufflinks RNAseq assembly suit (v2.2.1) (Trapnell et al., 2012) with geometric library normalization.

TTYH1-C19MC gene fusion break points were assessed based on concordance of and SNP array/Methylation array copy number analysis. RNAseq fusions breakpoints were called using TopHat-Fusion (v2.1.0). Paired-end reads were aligned to a GRCh19 reference genome using the following parameters specifically for finding fusion transcripts: –fusion-anchor-length 15 –fusion-min-dist 10000 –segment-length 50 –mate-inner-dist 0 –mate-std-dev 80. False positive from TopHat-Fusion were further assessed using TopHat-fusion-post by aligning the sequences flanking fusion junctions against BLAST (Basic Local Alignment Search Tool) databases (human genomic, other genomic and nt) and also manual inspection with Integrative Genomics Viewer (IGV) (v2.3.72).

Methylation and RNAseq Public Data

Additional methylation (GSE49377, GSE54719, GSE70460, GSE75153, GSE73801, EGAS00001000506) and RNAseq (SRP032476) data were downloaded from public resources.

H3K27Ac ChIPseq Sample Preparation and Analysis

Snap-frozen primary tissues were prepared for H3K27Ac ChIPseq analyses according to previously published methods (Mack et al., 2018). Briefly, formaldehyde cross-linked chromatin from 1E6 cells or 5 mg of snap frozen tumor samples were fragmented via water

bath sonication to ~200 bp fragments. Chromatin immunoprecipitation (ChIP) was performed using 5 μg of H3K27Ac antibody (#39133 Active Motif; CA, USA), which was pre-incubated for 6 hours with Dynabeads A and G (Invitrogen; CA, USA) and rotated overnight at 4°C. Antibody-free chromatin was retained as input control. Chromatin was de-crosslinked using 1% SDS and 0.1 M NaHCO3 and DNA was purified using QIAGEN QIAquick PCR purification kit (Cat # 28104), and quantified using PICO green. DNA libraries were prepared using NEB Next ChIPseq Illumina Sequencing library preparation kit. Samples were barcoded using NEB Next Barcodes (New England Biolabs; ON, Canada) and pooled in equimolar amounts. Sequencing was performed using pair-end 50 bp reads on the Illumina HiSeq 2000 sequencing (Beckman Coulter; MA, USA). Peaks were called using the MACS2 software (v2.1.0.20140616) (Zhang et al., 2008).

ATACseq Sample Preparation and Analysis

Snap-frozen primary tissue was prepared for ATACseq according to previously published methods with minor modifications (Buenrostro et al., 2015). Briefly, nuclei were prepared from ~50,000 cells by spinning at 600 x g for 10 min, followed by a wash using 50 μl PBS buffer, and further centrifugation at 600 x g for 5 min. Cells were lysed using cold lysis buffer (10 mM Tris -HCl, pH 7.4, 10 mM NaCl, 3 mM $MgCl_2$, 0.1%), and subsequently centrifuged for 10 min at 600 x g at 4°C. The supernatant was removed and pellet re-suspended in 50 μl of transposase mix (25 μl of 2xTD Buffer, 2.5 μl of transposase (TD enzyme; Illumina), 22.5 μl of water) for 30 min at 37°C. Next, library amplification was performed using the NEBnext High Fidelity 2xPCR Master Mix (Cat#M0541S) according to previously published PCR conditions (Buenrostro et al., 2015). PCR reactions were purified using QIAGEN miniElute kit, and a following size selection step was performed using LabChip (Cat#760601). ATACseq library preparations were sequenced using single-end 50 bp reads on the Illumina HiSeq 2000 platform. Raw reads were adapter-trimmed using Trim Galore (v0.2.5) and aligned to the genome with Bowtie (v1.0.1) with the m1 option enabled to allow for only uniquely aligned high-quality reads. Peaks were called using the MACS2 software (v2.1.0.20140616) (Zhang et al., 2008) with the options –q 0.05 to retain significant peaks, –shiftsize 50 to account for the transposase fingerprint, and otherwise default parameters were used.

Mapping Long Range Enhancer Interaction Using C3D

We applied Cross Cell-type Correlation in DNase I hypersensitivity (C3D) analysis, which calculates correlations between open regions of chromatin based on DNase I hypersensitivity signals or ATAC sequencing (Mehdi et al., 2018), to ATACseq data from 5 ETMRs to confirm presence of the *TTYH1-C19MC* gene fusions and discover long range MYCN promoter-enhancer interactions using prior published methods. C3D analyses performed with the MYCN promoter (Chr2:16,079,544-16,080,544) as an anchor ($R > 0.4$, $p < 10^{-10}$) identified 173 interacting regions ($R > 0.4$, $p < 10^{-10}$) on chromosome 2 that mapped at least 1 Kb outside of gene bodies in at least 1/5 ETMRs; 13 interacting regions which were identified in 4/5 ETMRs were further narrowed down to 5 candidate enhancer regions based on overlap with H3K27Ac ChIPseq Broadpeaks ($p < 0.01$) in 5/5 (Table S6). Further analyses showed that the 5 open enhancer regions, which mapped in a gene desert upstream of MYCN promoter, only correlated with expression of MYCN while *GACAT3*, the only other gene residing in the region of predicted DNA looping, is not expressed in ETMRs (average FPKM = 0.21198).

Additionally, results from a separate C3D analysis performed using ATACseq data from 2 ATRT primary tumors and MYCN promoter as an anchor revealed 4 interaction regions ($R > 0.4$, $p < 10^{-10}$) that mapped to chromosome 2 in at least 1/2 tumors. 1 region (Chr2:2617107-2617587) overlapped with H3K27Ac ChIPseq Broadpeaks ($p < 0.01$) to reveal a putative long-range enhancer. C3D analysis on ETMRs using the LIN28A promoter (Chr1:26,737,148-26,738,148) as an anchor only revealed 1 possible interaction in 1/5 ETMR primary tumors. C3D analysis of the *C19MC* enhancer (Chr19:54164387-54168379) revealed 192 DNA-DNA interactions within a 1.5Mb window. Subsequent analysis focused on statistically significant interactions ($q < 0.05$). All correlations were tested for statistical significance and adjusted for multiple testing (FDR) within the 1.5 Mb window. Correlation matrices were generated using the corrplot R package (Wei and Simko, 2013).

Core Regulatory Circuitry (CRC) Analyses

H3K27Ac ChIPseq peaks were calculated for 5 ETMR tumors using the MACS2 algorithm (Model-Based Analysis of ChIPseq). A q-value threshold of enrichment of 1×10^{-5} was used for all data sets. Super-enhancers were identified using the ROSE (Rank Ordering of Super-Enhancers) algorithm (Whyte et al., 2013) based on the H3K27ac ChIPseq signal with the default parameters. MACS2, ROSE output and RNAseq values (FPKM >1) were used to identify the core master TFs using CRC mapper (Saint-Andre et al., 2016). The algorithm identified 190 putative master TFs (Table S7), which were narrowed down based on chromatin accessibility using ATACseq data (q value <0.05), high RNA expression (FPKM >20) and upregulation in hNSC6-5mir vs. control to 18 TFs (Table S7). Master TFs were further narrowed down on positive correlation (R-value) between RNAseq values of each putative TF correlated with average *C19MC* miRNA expression using Nanostring data. The TF list was then overlapped with genes that were upregulated in hNSC6-5miR vs hNSC6-pcDH. Finally, we overlapped TF list with genes that were upregulated in A664-5miR compared to A664-pcDH and also significantly up-regulated in ETMRs compared to other PBTs using RNAseq data ($q < 0.05$).

Super-Enhancer Pathway Analysis

ROSE algorithm identified 1330 super-enhancers that were present in at least 1/5 tumors. The output was annotated using a custom script that assigned super-enhancer regions to the nearest highest expressed gene within a 100 Kb window. List of super-enhancers were input into gProfiler (Reimand et al., 2016) and pathways were selected using FDR<0.01 and visualized using the Enrichment Map application (Merico et al., 2010) for Cytoscape (Shannon et al., 2003).

DATA AND SOFTWARE AVAILABILITY

The accession number for the ETMR RNAseq, H3K27Ac ChIPseq, ATACseq, Nanostring, methylation, SNP genotyping array and LIN28A RIPseq data reported in this paper is EGA: EGAS00001003437 and can be reached through this link: https://www.ebi.ac.uk/ega/studies/EGAS00001003437.

QUANTIFICATION AND STATISTICAL ANALYSIS

Kruskal-Wallis test was used to assess significance of gene expressions between ETMR and other PBTs, as well as between *C19MC* amplified and gained tumors. A two-tailed student t-test was used to calculate significance for all cellular and biochemical assays. A p value of <0.05 was regarded as significant for all analyses. Statistical significance and number of replicates indicated in figure legends. Error bars shown as Standard Error of Mean (SEM). Benjamin-Hochberg correction method was used to calculate q values from H3K37Ac-ChIPseq and ATACseq peaks relative to input control sample. All analyses were conducted in the R statistical environment (v2.15.2) or with the GraphPad Prism 7.0 software.